Re-thinking polyamide thin film formation: How does interfacial destabilization dictate film morphology?

Ines Nulens [a,1], Adi Ben Zvi [b,c,1], Ivo F.J. Vankelecom [a], Guy Z. Ramon [b,c,d,*]

[a] Membrane Technology Group (MTG), Centre for Membrane Separations, Adsorption, Catalysis and Spectroscopy for Sustainable Solutions (cMACS), KU Leuven, Celestijnenlaan 200F Box 2454, Leuven, 3001, Belgium
[b] Department of Civil and Environmental Engineering, Technion—Israel Institute of Technology, Haifa, 320000, Israel
[c] Nanoscience and Nanotechnology Program, Technion-Israel Institute of Technology, Haifa, 32000, Israel
[d] Wolfson Department of Chemical Engineering, Technion—Israel Institute of Technology, Haifa, 320000, Israel

ARTICLE INFO

ABSTRACT

Unravelling synthesis-morphology-performance relations of thin-film polyamide (PA) selective layers prepared via interfacial polymerization (IP) is essential for tailor-made membrane design. Here, an approach is outlined, which links synthesis and morphology in terms of the interfacial stability of a system undergoing IP, with the notion that a transition from a stable to an unstable state corresponds to a morphological shift of the resultant film, e.g., from smooth to crumpled. Within the proposed framework, physical parameters related to a variety of synthesis conditions are identified and classified based on their effect on two defined criteria: the polymer formation rate and/or the system susceptibility to instability. A conceptual phase diagram maps the morphological regimes with respect to the relevant parameter space. Our analysis, based on available literature data, illustrates how PA morphology, as observed in published SEM images, transitions from smooth to crumpled, exhibits a remarkable correlation with the defined parameter space, and hereby the stability of the system. Re-thinking experimental results in this manner highlights not only the underlying physics, but also identifies potential pitfalls when variations of synthesis conditions result in conflicting effects. Our motivation is to encourage experimental design based on the developed framework supplemented by theoretical quantification, which will strengthen the fundamental understanding of IP for a given chemistry, with the goal of providing a clear physical toolbox for IP-based membrane design.

1. Introduction

Membrane-based desalination via reverse osmosis (RO) has become the prevalent technology for producing high quality water from a variety of feed streams, ranging from seawater to wastewater [1–6]. Fully aromatic polyamide thin film composite (TFC) membranes, fabricated by interfacial polymerization (IP), have become the state-of-the-art for RO due to their unrivaled performance, with NaCl rejection >98% and water permeance of ~4 $Lm^{-2}h^{-1}bar^{-1}$ and 1 $Lm^{-2}h^{-1}bar^{-1}$ for brackish water and seawater RO respectively [1,7–10]. However, much can still be improved, as these membranes have high propensity to foul [11,12], are sensitive to oxidation [13,14], have insufficient rejection of chemicals of concern for human health and agriculture such as boric acid and micropollutants [15,16] and show a trade-off between permeability and

selectivity [17,18]. Improvements will also further push the applicability of these TFC-membranes in other fields, such as gas separation [19], solvent resistant nanofiltration [20–22] and flow batteries [23, 24]. Understanding the intricacies of the IP process and its impact on the resultant synthesis-morphology-performance relations is essential in the quest for improved membrane design for specific applications as well as facilitating replacement of currently used hazardous chemicals with alternative, green materials [1,14,25–29].

1.1. Interfacial polymerization

Polyamide TFC membranes generally comprise a thin, selective polyamide layer (overall thickness <250 nm) on top of a porous polymeric support. The dense, cross-linked selective layer is synthesized via

a fast and exothermic Schotten-Baumann polycondensation reaction of two polyfunctional monomers, separately dissolved in immiscible solvents. The reaction occurs at the interface, hence the name IP (Fig. S1) [30,31]. The most common monomers and solvents involved in the reaction are the trifunctional acyl chloride, trimesoylchloride (TMC), dissolved in hexane, while in the aqueous phase either m-phenylene diamine (MPD) is used for RO membranes, or piperazine (PIP) for NF membrane preparation [29,32–34]. Owing to the better solubility of the amine monomer in the organic phase and the high intrinsic reaction rate, the reaction usually occurs on the organic side, near the interface, and is therefore diffusion limited. During the reaction, the pH of the aqueous solution decreases as MPD is consumed and HCl, a by-product of the reaction, is released. Some of the MPD becomes protonated as it reacts with HCl. This protonated form is no longer reactive towards the acyl chloride, so IP cannot be performed [33,35]. IP can be executed using a wide variation of synthesis parameters that affect the film morphology (geometry, void size and interconnectivity, intrinsic thickness, surface area) and chemical characteristics (size of aggregate, network pores, and charge) which are intrinsically linked with membrane performance [25–29,77–82]. Literature that explores these relations is extensive, with commonly altered synthesis parameters being: monomer type [36–40] and concentration [22,30,41], reaction time [42,43], solvents used [44] and - perhaps the most varied – additives of various kinds: surfactants [45–48], co-solvents [47,49,50], and pH regulators [47,51,52]. Further alterations consist of different types of support layers [33,53–57] as well as recently explored inventive IP configurations [9,22,41,58–63].

These altered synthesis conditions have different and sometimes multiple physical effects on IP that are not well understood yet, since a thorough physical/mechanistic explanation for the synthesis-morphology-performance relationship is lacking [29,64]. As a result, most studies are empirical in nature and contradicting observations concerning membrane morphology and performance sometimes appear [58,65–69]. This knowledge gap is a direct consequence of the nature of IP, which is very challenging when seeking detailed (in-situ) characterization, i.e. due to its high polymer formation rate, the small spatial scale of the reaction, and the rough and heterogeneous nature of the resultant film [29,70–76].

1.2. The link between synthesis conditions and morphology – the stability concept in IP

In search of a theoretical description for the synthesis-morphology relationship, multiple pathways have been proposed that ascribe the origin of morphological features to the heat release and acid production throughout the IP reaction, as well as the fact that the polymer formation is never completely homogeneous over the interface [71]. Ukrainsky and Ramon directly measured the temperature increase at the interface during IP, and suggested that the observed temperatures are sufficiently high so as to cause solvent vaporization, particularly of the organic phase, as well as release of dissolved gasses, which may result in trapped bubbles within the forming polyamide film [29]. This was corroborated experimentally in a series of papers examining the 'nano-foaming' theory [30,83–85] that attributes the nanosized voids in the rough PA morphology to nanobubbles formed by dissolved gasses in the aqueous phase, due to temperature increase and/or pH decrease during the reaction [30]. More recently, Peng et al. [86] showed that employing organic solvents with higher vapor pressures resulted in larger nano-voids within the polyamide top-layer. Song et al. [87] further refined the ridge and valley formation mechanism by suggesting that confinement by a support plays an important role. However, since using higher monomer concentrations or longer reaction times can also induce rough surface morphologies in the case of SFIP, as seen in the papers of Karan et al. [9] and Cui et al. [58], the strict requirement of confinement by a support is questionable.

The above-mentioned mechanisms are driven by temperature and/or compositional changes of the system, in response to IP, and can be considered as subsets of a more generalized concept – instability - defined as the inability of a system to sustain itself against small perturbations. Such perturbations exist naturally, e.g., due to temperature fluctuations. In a stable system, these perturbations are dampened and decay in time; conversely, when these perturbations are amplified (usually due to some positive feedback in the system) and continue to grow, the system becomes unstable [88]. Karan et al. [22] were the first to mention interfacial instabilities, Rayleigh-Bénard convection, as a possible cause for crumpling of the PA film. Recently, Freger and Ramon [71] outlined a set of instability mechanisms that can be linked to IP, such as thermo– and soluto-capillarity, bubble formation, elastic crumpling and fluid shear. Thermo- and soluto-capillary instabilities arise due to gradients in temperature and solute concentration along a liquid-liquid interface, respectively, that act as perturbations. Both result, in turn, in gradients of interfacial tension at the liquid-liquid interface that induce capillary flow from lower to higher interfacial tension regions, known as Marangoni flow. Such hydrodynamic instabilities may result in interfacial deformation when the shear exerted by the flow exceeds the surface tension, which may cause crumpling of the forming film. Fluid shear, due to relative motion of the phases in a roll-to-roll process, may also result in an instability leading to a deformed film [89]. Elastic crumpling of the formed film may occur when the film experiences gradients in temperature and therefore expands in a non-uniform way, resulting in a crumpled morphology. Finally, differential thermal expansion of the polyamide film and the polymeric support due to temperature gradients can induce local detachment of the polyamide film followed by crumpling.

Despite the mentioned efforts, a physics-based framework linking synthesis conditions and film morphology has not yet been established. The present work is therefore aimed at laying the foundations of such a framework, by classifying synthesis conditions according to their underlying physical effects affecting the stability of an IP system. This proposed framework draws on well-established concepts of hydrodynamic stability theory, to show how a chosen set of synthesis conditions determines the final film morphology. The validity of the framework is illustrated via analysis of compiled literature data. Overall, this work aims at establishing an improved, unified picture of the synthesis-morphology relationship of polyamide TFC membranes.

2. The proposed framework

2.1. Transition from smooth to crumpled

When observing the top-layer morphologies of polyamide TFC membranes reported in literature, a clear evolution of the morphology is seen, from almost completely smooth to multilayered. Here, five defined categories are applied: smooth – nodular - nodules and leaves – ridge and valley – multilayered, as illustrated in Fig. 1.

For simplicity, the categories nodular, nodules and leaves and ridge and valley are merged in this study into one overarching category termed 'crumpled', whenever the more specific differentiation is not required. In what follows, the three categories are represented by symbols: a green circle (smooth), a yellow diamond (crumpled) and a red triangle (multilayered). The characterization is based on visual inspection: smooth films have little or no protuberances, with an RMS roughness <40 nm [9,30,62,83], crumpled films are defined by surface morphological features that are spread relatively homogeneously and with an RMS roughness of 30–100 nm [9,83], while multilayered morphologies are characterized by relatively low RMS values, due to 'bent-over' leaves covering the underlaying morphological features. These films can be clearly distinguished from smooth films by visual inspection of SEM and TEM images. The morphological discussion in this work is based on SEM images of membrane surfaces, not cross-sections, since surface images are more generally available. Whenever available, cross-sectional SEM/TEM images of the examples
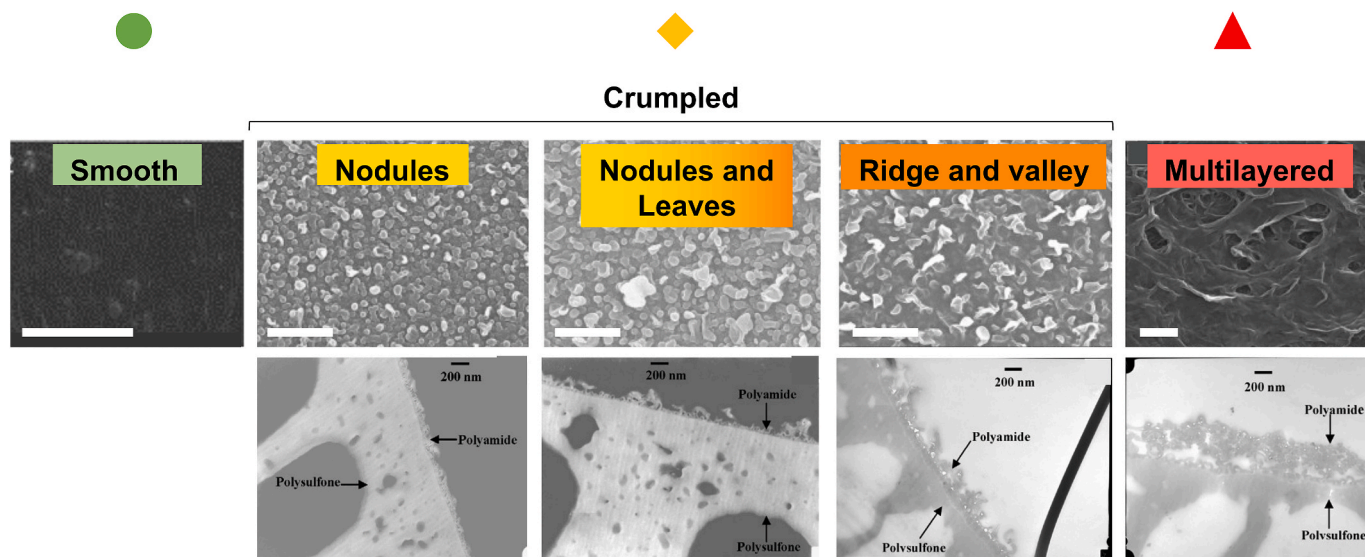
Fig. 1. Different morphological features of polyamide thin films, shown as transition from smooth to multilayered. TOP: top-view SEM images of smooth [30], nodules [44], nodules and leaves [44], ridge and valley [44] and multilayered [90] morphologies. BOTTOM: cross-sectional TEM images of nodules, nodules and leaves, ridge and valley and multilayered morphologies [44]. In all images, the scale bar is 1 μm. Smooth morphology is represented in the figures below by a green circle, crumpled morphology includes the categories: nodules, nodules and leaves, and ridge and valley, and is represented by a yellow diamond. Multilayered morphology is represented by a red triangle. (For interpretation of the references to color in this figure legend, the reader is referred to the Web version of this article.)

used in the text are provided in the SI.

2.2. From synthesis conditions to film morphology

Within the framework outlined hereinafter, the IP reaction is considered as a system, defined by the various aspects of the set-up used to execute IP, including variables such as: monomer concentrations, solvents, temperature, support characteristics, coating method, etc. All these variables, also referred to as synthesis conditions, are reduced to their physical meaning/attributes relevant to IP (Fig. 2). Together, these physical attributes define the parameter space in which the IP system is executed, which is then classified into two categories used to define the system's stability, namely the *polymer formation rate* and the system's *susceptibility to instability* (section 2.2.2). The hypothesis is that these two categories may be used to describe the transition from a smooth film, reflective of a stable state, to a crumpled/multilayered structure, reflective of an unstable state – governed by different instability mechanisms (section 1.2 and 2.2.1) triggered during film formation.

### 2.2.1. Instability mechanisms causing film crumpling during IP

Soluto- and thermo-capillarity, as well as bubble formation, are probable mechanisms that can destabilize an IP system and deform the interface, resulting in the film's morphological features, due to the evolution of interfacial temperature and/or concentration gradients or pH decrease (see Fig. 3 and section 1.2). Destabilizing properties of IP

within this respect are the high reaction rate, exothermic nature, acid formation and spatial heterogeneous growth (section 1.2). System properties such as thermal conductivity and diffusivity, on the other hand, act as stabilizers as they reduce gradient formation. Using the terminology of stability theory, the spatial distribution of the different gradients can be considered as a set of 'wavelengths' of hydrodynamic disturbances.

In the case of soluto- and thermo-capillarity, Marangoni flow could be generated in either or both the aqueous and organic phase (where the reaction usually takes place) of the interface. Key physical attributes with respect to soluto- and thermo-capillarity are thus: the solvent viscosities, solvent mass and thermal diffusivities and the interfacial tension between both liquid phases (see definition of Marangoni number [91], equation S(1) in SI). Furthermore, key physical attributes with respect to bubble formation are the concentration of dissolved gases and the solvents' boiling points/vapor pressures.

In the presence of a support, polymer growth will be more spatially heterogeneous due to the distribution of pore location and sizes, as well as surface roughness, manifesting itself as inherent geometrical disturbances in the system (much like a rough wall of a pipe can trigger the transition from laminar to unstable flow). Consequently, larger interfacial gradients and higher differences in the bubbling rates will evolve along the interface, resulting in a higher probability to form morphological features (see Fig. 3).

In conclusion, the more intense and spatially heterogeneous the
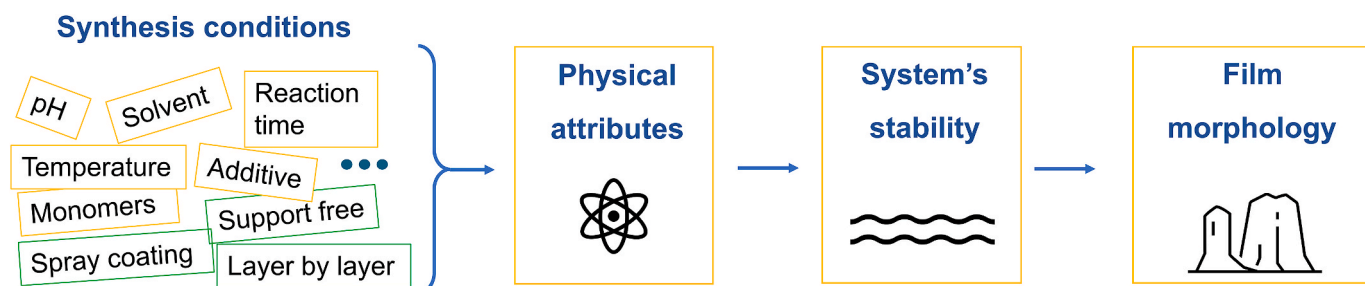
Fig. 2. Schematic overview of the framework for the synthesis-morphology relationship introduced in this work.
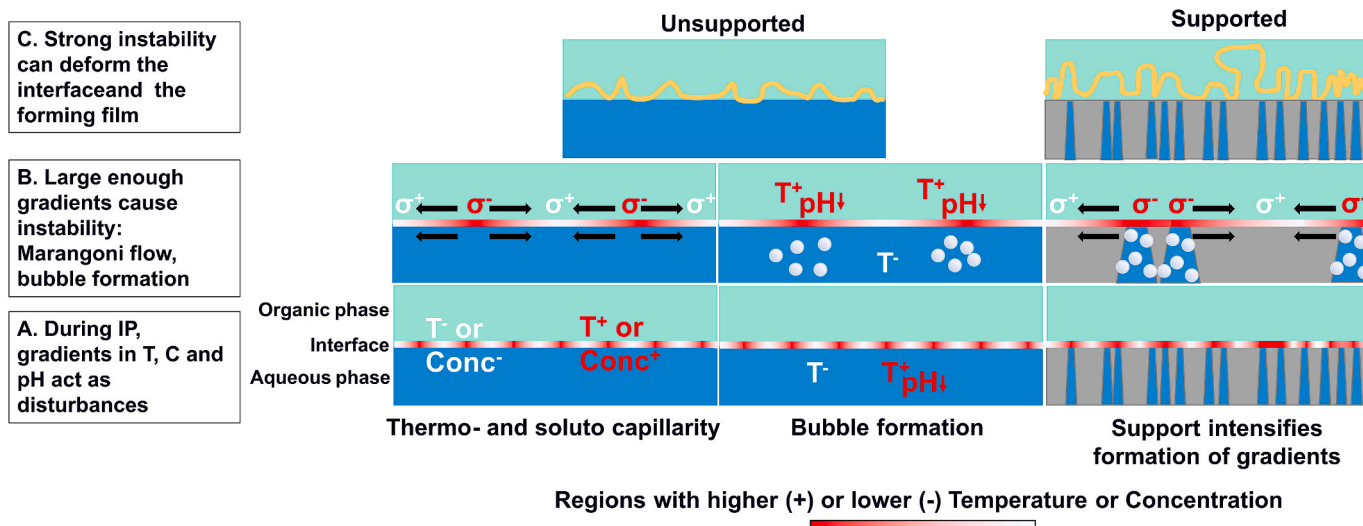
Fig. 3. Schematic representation of interfacial destabilization during IP due to thermo- and soluto-capillarity and bubble formation for a supported and unsupported system. Thermo- and solute capillarity are illustrated by flow on the organic side and aqueous side of the interface (as a result of a gradient in interfacial tension, σ). Bubble formation is illustrated in the aqueous phase by means of degassing of dissolved gases (e.g. CO_2). Bubble formation could, however, also occur in the organic phase as a result of vaporization of the organic solvent, molding the film like foam. The magnitudes of temperature, concentration and pH gradients are larger in the case of a heterogeneity such as the presence of a support. Interface deformation will be more intense in this situation.

reaction is, the more probable that one of the instability mechanisms will be triggered, forming morphological features. Essentially, the generation of gradients (as a result of heterogeneous polymer growth) relies on the relative magnitudes of the reaction rate, the mass transfer rate within the system and rate of heat dissipation.
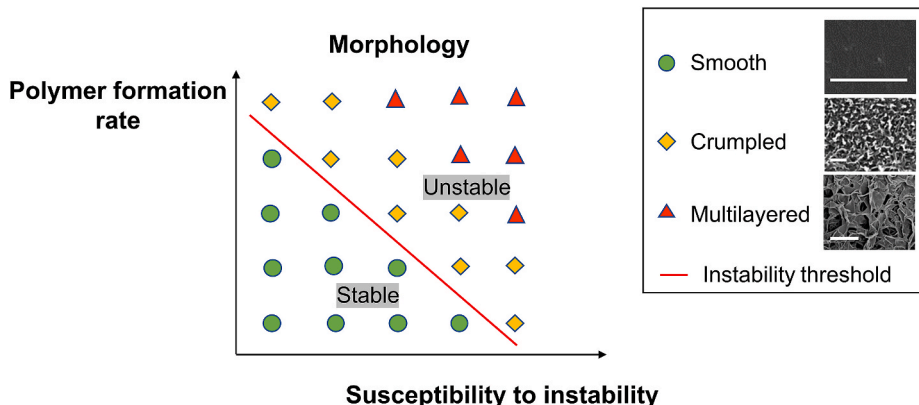
2.2.2. A conceptual phase diagram: linking system stability to resultant film morphology

In order to link the system stability to the resultant film morphology, a conceptual phase diagram is used (Fig. 4). The axes are the polymer formation rate and the system susceptibility to instability, defining the state of the system. The phase diagram is a useful way to visualize a two-dimensional parameter space, dividing it into regions (or regimes) that represent distinct states of the described system. In our case, a third dimension is added to the diagram by linking the different states to a morphological regime (smooth, crumpled, multilayered). The system states defined within the diagram are not necessarily thermodynamic equilibrium states, as several publications have shown that long reaction times (say hours) evoke a transition to rough surfaces even if the surface was smooth after 1 min of reaction time [58,92]. The motivation for this type of phase diagram was taken from physics, for example in fluid dynamics, where the critical Reynolds number is plotted versus the wavelength of the disturbance, mapping transitions between laminar

and transitional flow [93].

The system susceptibility to instability is the tendency of the system to become unstable. It defines how close the system is to its instability threshold. Thus, as the system's susceptibility to instability is higher, a lower energy input (or a weaker perturbation) is required to shift the system from a stable into an unstable state. The energy input required corresponds, in this case, with the polymer formation rate. The interplay between the two properties: 'polymer formation rate' and 'system susceptibility to instability' thus defines whether the system will become unstable and to what extent. The degree of instability then dictates the resultant film morphology, expressed qualitatively by the symbols defined in section 2.1. A smooth film is formed if the system remains stable throughout the reaction. A progressively more unstable state throughout the reaction corresponds to the different subdivisions of the crumpled morphology (Fig. 1) and finally, the most unstable state results in the multilayered morphology. The transition from smooth to crumpled morphology requires crossing the instability threshold, illustrated by a red line on the phase diagram. The formation rate and the system susceptibility were selected as the main determinants for the system stability as they both fuel the instability mechanisms described in section 2.2.1.

2.2.2.1. Polymer formation rate. The y-axis of the phase diagram is

Fig. 4. Stability-morphology relationship in IP. A conceptual phase diagram linking the polymer formation rate and the system's susceptibility to instability of the IP system that corresponds with morphological features of the film (for simplicity categorized as 'smooth', 'crumpled', and 'multilayered'). If the system crosses its instability threshold, a crumpled morphology evolves. The different morphological states are represented by the following symbols: green circles for smooth films, yellow diamonds for crumpled films, and red triangles for multilayered films. SEM images are taken from: Ma et al. [30], Hermans et al. [52], Xu et al. [65]. Scale bar is 1 μm. (For interpretation of the references to color in this figure legend, the reader is referred to the Web version of this article.)

represented by the polymer formation rate - the speed of the reaction. Higher rates imply higher concentrations and higher generated amounts of heat and acid, manifested in larger gradients of concentration, temperature and pH. Hence, as the polymer formation rate increases, destabilization of the interface becomes more probable as is the formation of morphological features (illustrated in Fig. 4).

The polymer formation rate can be simplified and lumped into two factors: the 'initial amine flux' and the 'sustainment of the reaction', as shown in Fig. 5A. The former is an 'initial' parameter, in that it is defined by the initial state of the system, while the latter is a 'dynamic' parameter, that changes during the reaction due to acid and heat release (as a consequence of monomer consumption). It was chosen to distinct between the initial state and dynamic character of IP since it was experimentally shown that IP systems will result in rough morphologies over time if the system is left to react and monomers remain supplied, irrespective of the extent of the initial amine flux [29,58,92,94]. Therefore, even a stable system, say a film which remains smooth after 1 min of reaction time, will evolve into a rough film over longer reaction time (i.e. if the sustainment of the reaction is increased).

The initial amine flux, J_0 (mol/m^2.s), may be derived, approximately, from a mass balance considering the diffusive flux and the reaction (see, e.g., Freger [95] and Nowbahar et al. [70]). As such, it may serve as a quantitative proxy for the initial polymer formation rate, since it scales with the monomer consumption during the initial stage of the reaction [70]. Under these conditions, it may be estimated as [70,95]:

$$J_0 = K[MPD]_0 \sqrt{6k[TMC]_0 D}, \qquad (1)$$

in which K is the partition coefficient of MPD, $[TMC]_0$ and $[MPD]_0$ denote initial bulk concentrations of the monomers in the organic and aqueous phases, respectively, D is the diffusivity of MPD in the organic phase, and k is the reaction rate constant. The initial amine flux is based on the actual concentrations of the monomers in the reaction zone. It

thus largely depends on the affinity of the amine for the organic phase, the reactive monomer bulk concentrations and monomer diffusion in the organic phase, which are directly affected by the following physical attributes (see Fig. 5A). First, the amine affinity for the organic phase will increase as the interfacial tension decreases (with the exception of interfacial tension variations induced by surfactants), manifested by a higher equilibrium partition coefficient of MPD in the organic phase. Second, the diffusive flux is a parameter affecting both initial amine flux and sustainment of the reaction. It is affected by the solvent viscosities of both phases as well as the size of the monomer. Solvent viscosity, on the other hand, also affects the susceptibility to instability (see further discussion in the next section). Finally, it should be noted that the MPD concentration in the aqueous phase, used to calculate the initial amine flux, is the *unprotonated* fraction of MPD, which is the pH-depending reactive MPD concentration. This distinction is particularly important when the initial pH is adjusted (see details in SI).

The *sustainment of the reaction* represents the ability of the system to maintain polymer formation over time. For example, this can be achieved, in principle, as long as reactive monomers are supplied [29,92]. The sustainment depends on mass transfer of both monomers, in the liquid phases as well as through the forming film, and also on the total amount of reactive monomers available in the system (i.e. unprotonated MPD and unhydrolyzed TMC).

2.2.2.2. Susceptibility to instability. The x-axis of the phase diagram represents the system's susceptibility to instability. This is primarily defined by three factors (Fig. 5b): 1. the system's intrinsic heterogeneity, 2. the ease of interfacial deformation and 3. the potential for degassing and/or solvent vaporization. The first is solely related to the system's initial state (designated blue in Fig. 5b), while the latter two affect the susceptibility both initially as well as dynamically (designated as a blue-green gradient in Fig. 5b), that is, during the evolution of the reaction.

System heterogeneity is defined by the spatially heterogeneous
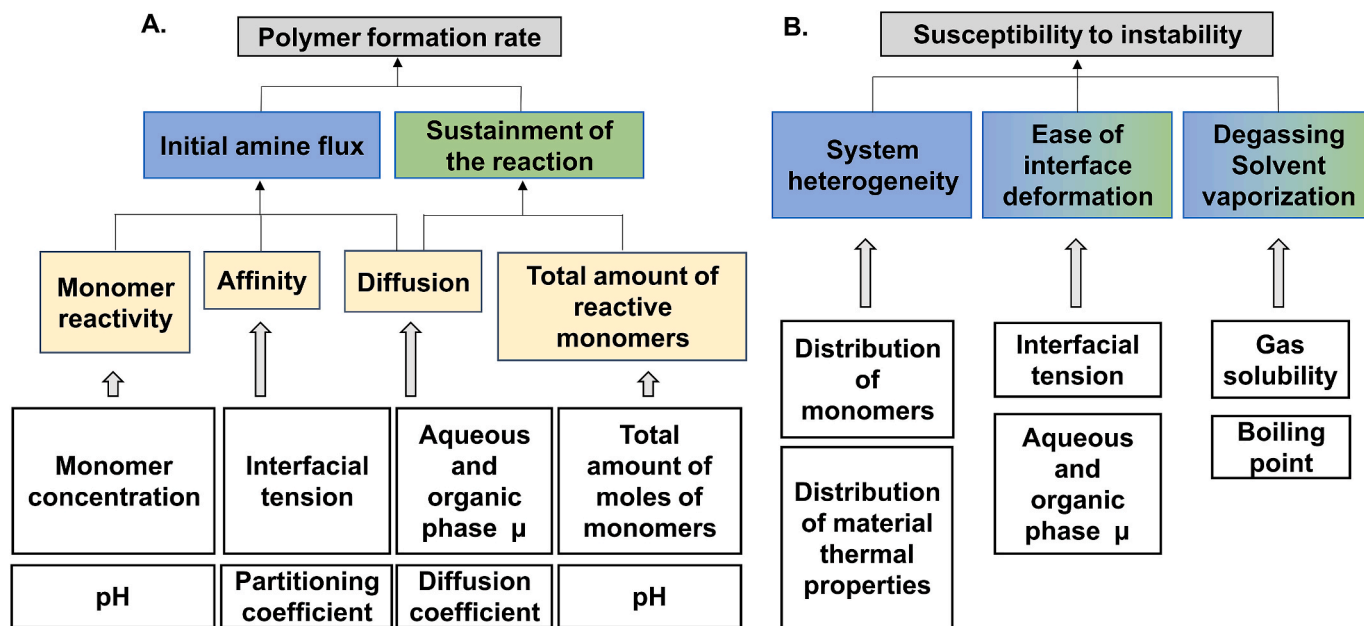
Fig. 5. Properties that impact the polymer formation rate (A.) and susceptibility to instability (B.). The polymer formation rate depends on physical parameters (yellow and white boxes) that mainly affect the initial amine flux and sustainment of the reaction, being: pH, interfacial tension, equilibrium partitioning coefficient, viscosity of both aqueous and organic phase, diffusion coefficient of amine in the organic phase and the total amount of monomers present in the system. The susceptibility to instability is reflected by physical parameters that mainly affect the system heterogeneity, ease of interface deformation and degassing and/or solvent vaporization, such as: interfacial tension, the distribution of monomers and local material properties, gas solubility and boiling point. Blue colored boxes indicate characteristics of the initial state of the system. Green colored boxes indicate characteristics that are altered once the reaction is started (dynamic). Parameters can be either initial and/or dynamic, if they are both initial and dynamic the box is colored in a blue-green gradient. This schematic is not meant to be inclusive of all physical parameters that might affect the polymer formation rate, but rather emphasizes the parameters that are considered of primary importance. (For interpretation of the references to color in this figure legend, the reader is referred to the Web version of this article.)

distribution of monomer concentrations and material's thermal properties, relevant when comparing different synthesis configurations such as supported and unsupported systems. The spatial monomer distribution refers to the pore size, porosity and pore distribution in case of a supported system. These characteristics can be further refined based on the notion that the porous morphology of the support serves as a 'wavelength' of the disturbance made to the initial state of the system.

The material's thermal properties refer to heat dissipation during IP executed on top of a support, which is more heterogeneous compared to an unsupported system (see Fig. S2). A thin water layer creates the interface with the organic phase on top of a support, connected with the aqueous phase within the support pores. Heat will be dissipated through the aqueous phase and the solid support matrix at different rates, facilitating the formation of temperature gradients in the supported case (Fig. S2). The thermal conductivity of water ($0.60 \ Wm^{-1}K^{-1}$) [96] is higher than that of polymers such as polysulfone ($0.26 \ Wm^{-1}K^{-1}$) [97] (and higher than the thermal conductivity of common organic solvents (hexane $0.12 \ Wm^{-1}K^{-1}$) [98], however this does not alter the spatial heterogeneity of heat dissipation). We note that comparing thermal conductivities may not provide an accurate assessment of relative heat dissipation through different materials, if the system is in a transient state (rather than a steady-state) during IP. In a transient situation, which would arise if the conduction time-scale is on the order of, or smaller than, the heat production rate, the materials' heat capacities and densities should be taken into account by comparing thermal diffusivities instead of thermal conductivities.

The ease of interfacial deformation depends primarily on the interfacial tension, which tends to minimize the interfacial area or, in the case considered, keep it flat. Low interfacial tension is less effective in dampening an induced disturbance of the system, making the interface easier to deform. However, the interfacial tension is also a dynamic property, since its quantitative value may deviate from its initial value over the course of the reaction (due to temperature and/or compositional changes). Since, in the case of a hydrodynamic instability, it is the flow that will drive the deformation, the solvents' dynamic viscosities can affect the deformation via their resistance to the flow. As with the interfacial tension, solvent viscosity is a dynamic property.

Finally, the potential of a system to undergo bubble formation via degassing and/or solvent vaporization enters the definition of a system susceptibility to instability. The potential for degassing is defined by the solubility limit of the relevant gas (e.g. CO_2) and the amount of soluble gas initially dissolved in the aqueous phase, while the choice of solvent dictates whether its boiling temperature would be higher or lower.

The utility of the phase diagram may be described as follows: depending on the synthesis conditions, the system is located either in the stable region, closer to or away from the instability threshold, or it may be in a region already marked as unstable, to varying extents. Whether a system is unstable and to what extent, depends on the interplay between both initial and dynamic properties of the reaction (blue and green boxes in Fig. 5), expressed as the increase on the x-and/or y-axes of the phase diagram (Fig. 4). So, if one has either a physical model capable of making the stability analysis, or experimental data that covers the
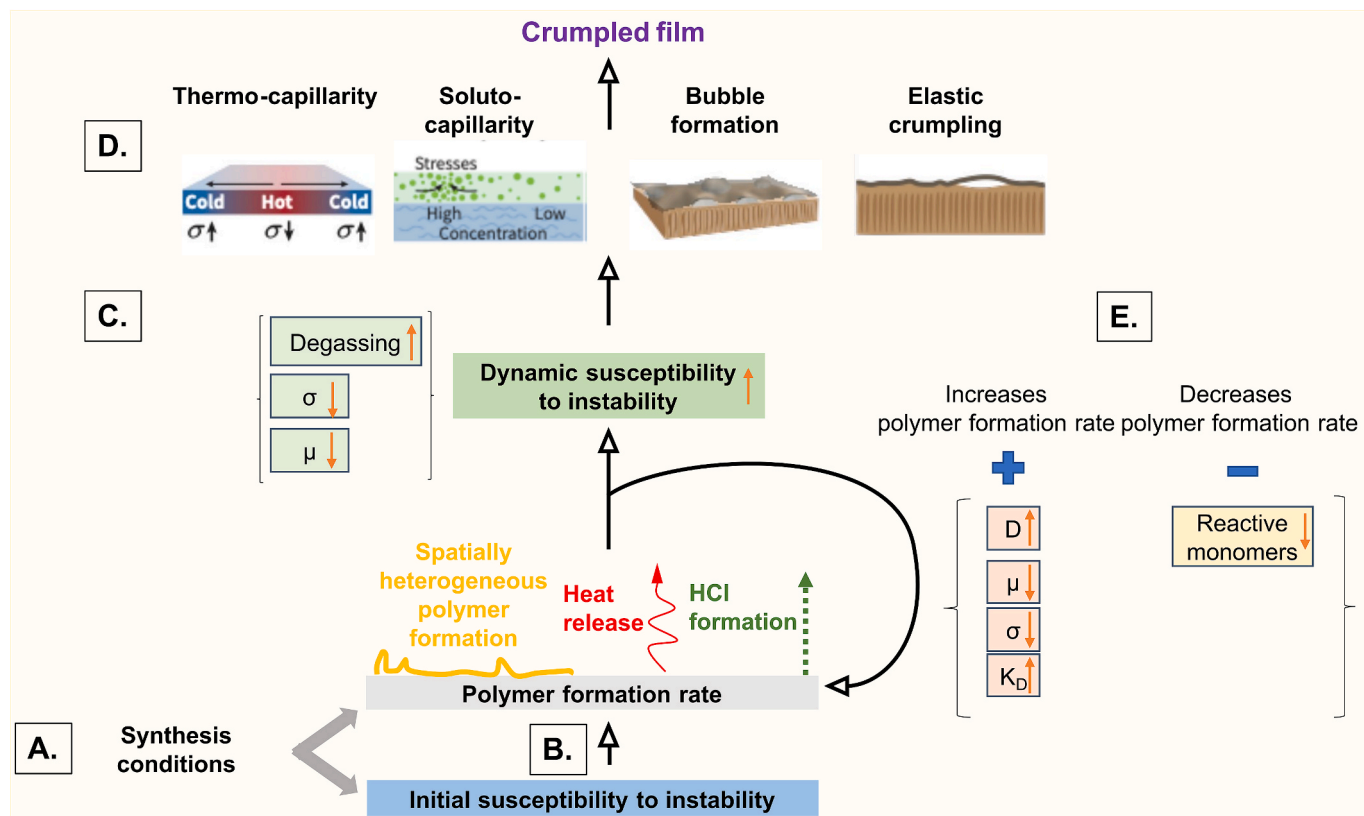
Fig. 6. The 'feed-back' loop of the polymer formation rate through the evolution of IP, and its link to instability that ultimately leads to a crumpled film morphology. (A.) The chosen synthesis conditions define the system initial susceptibility to instability (blue) as well as the initial polymer formation rate (grey). (B.) The system heterogeneity, part of the system initial susceptibility to instability, will dictate how heterogeneous in space the polymer formation will occur initially (yellow). Once the reaction is initiated, heat release (red) and HCl formation (dark green) will occur in a spatially heterogeneous fashion in continuation of the system initial state. (C.) Consequently, physical characteristics within the system will vary accordingly: enhanced degassing, decreased interfacial tension (σ) and viscosity (μ) (light green boxes) will increase the susceptibility to instability leading to various instability mechanisms and to the formation of (D.) a crumpled film. (E.) The polymer formation rate will be affected in two ways: increasing due to decreased σ, increased monomers' diffusion coefficients (D), decreased solvent viscosity (μ), increased MPD partitioning coefficient (K_D), (orange boxes) and decreasing due to decreased concentration of reactive monomers (yellow box). (For interpretation of the references to color in this figure legend, the reader is referred to the Web version of this article.)

various regimes, a prediction may be made whether a given system would yield a given morphology – the ultimate goal of this framework.

The relation between IP reaction, the instability mechanisms and resultant film morphology can also be represented graphically from a mechanistic point of view (Fig. 6). The chosen synthesis conditions dictate the initial susceptibility to instability of the system as well as the initial polymer formation rate (Fig. 6A). Once the reaction is started, the system heterogeneity, part of the initial susceptibility to instability (Fig. 5b) enhances the spatial heterogeneity of the polymer formation rate (Fig. 6B) which results in perturbations of the system by means of temperature, concentration and pH gradients. Changes of the latter three parameters alter the dynamic susceptibility to instability of the system as interfacial tension and viscosities decrease and degassing and solvent vaporization are favored. These effects make the system more prone to be destabilized by several instability mechanisms (Fig. 6C) and form a crumpled morphology (Fig. 6D). The induced perturbations may grow or decay over time due to both positive (self-sustaining) and negative (self-inhibiting) feedbacks owing to the exothermic and acid releasing nature of IP (Fig. 6E) and further alter the dynamic susceptibility to instability. Indeed, heat release during IP, leading to a temperature increase, enhances mass transport of both monomers into the reaction zone since diffusion rate and partitioning coefficient of the amine increase and solvent viscosity and interfacial tension decrease. Enhanced mass transport will further increase the polymer formation rate, thus further intensifying temperature and pH gradients, feeding the instability mechanisms. The opposite is true for the decreasing pH during IP since amine monomers in the bulk aqueous solution become protonated, hence reducing the overall MPD reactivity and polymer formation rate.

2.2.3. Physical attributes of synthesis conditions

The final part of the puzzle is to link synthesis conditions with their physical attributes relevant to IP. The common way to think about adjusting the reaction conditions when performing IP is to classify the so-called 'synthesis parameters' into categories such as: monomer concentration(s), temperature, pH, buffer capacity, additives (e.g., (co-)/solvents, surfactants), coating technique, support properties, dissolved gases and side reactions. While this is a popular way of grouping the synthesis parameters, as it communicates directly with the 'recipe' to be used in membrane preparation, it does not completely relate to the physical effects these parameters have on the actual process. Here, we suggest to shift the emphasis towards categorization of synthesis parameters based on their physical effects, namely the changes imparted to

interfacial tension, monomer partitioning coefficient, pH, viscosity, diffusion coefficient, reactive monomer concentrations, distribution of monomers, distribution of material's thermal properties, gas solubility and solvent boiling point (cfr. Fig. 5). Commonly used synthesis parameters may thus affect a single or, in some cases, several aspects of the reaction (following the tree structure of Fig. 5). The link between synthesis conditions and their effect on polymer formation rate and system susceptibility to instability is summarized in Fig. 7. Here, the term 'coating technique' refers to the different preparation methodologies. Along with the conventional, supported system, are added unsupported, spray-assisted IP and layer-by-layer deposition, which are coating techniques that have been gaining ground in recent years. These techniques affect the distribution of monomers and material thermal properties as well as the total amount of reactive monomers present in the system (cfr. Section 2.2.2). Side reactions typically refer to the hydrolysis of TMC but can also include any other reactions that are initiated alongside the reaction between MPD and TMC. One example is the addition of chlorosilanes to the organic phase as demonstrated by Zhang et al.(2020) [51]. Once in contact with water, chlorosilanes hydrolyze in a highly exothermic and acid generating reaction. This specific example affects both pH and temperature (and, therefore, interfacial tension, partitioning coefficient, viscosity, diffusion coefficient, pH and gas solubility).

3. Analysis of literature results

3.1. Controlled increase of polymer formation rate or susceptibility to instability

After establishing the proposed theoretical framework describing the synthesis-morphology relationship of PA TFC membranes, the framework was applied to literature data. Studies were selected that varied specific synthesis conditions while keeping other variables constant. The synthesis conditions were first reduced to their physical attributes relevant to IP (cfr.Fig. 5). The magnitudes of the physical attributes were then translated to their effect on polymer formation rate and susceptibility to instability. Subsequently, the resultant film morphologies were examined. Together with the predicted effect on polymer formation rate and susceptibility to instability, the series of morphologies were interpreted in terms of degrees of the system stability (cfr.Fig. 4). As introduced in section 2.2.3, synthesis conditions can affect multiple physical attributes that can both affect polymer formation rate and system susceptibility to instability which makes a representation on the phase

Synthesis conditions	Polymer formation rate		Susceptibility to instability		
	Initial amine flux	Sustainment of the reaction	System heterogenity	Ease of interface deformation	Degassing vaporization
Monomer concentration	+	+			
Temperature	+	+		+	+
pH	+	+			+
pH buffer		+			+
(Co-)solvents	+	+		+	
Surfactants	+			+	
Coating technique		+	+		
Support properties		+	+		
Dissolved gases		+			+
Side reactions		+			+

Fig. 7. Classification of synthesis conditions according to their effect on the polymer formation rate (expressed by initial amine flux and sustainment of the reaction) and the susceptibility to instability (expressed by system heterogeneity, ease of interfacial deformation, and degassing and/or vaporization). The classification and color codes are based on the physical parameters that affect the synthesis conditions, as defined in Fig. 5 (blue – initial characteristics, green-dynamic characteristics, and blue-green gradient - both initial and dynamic characteristics). (For interpretation of the references to color in this figure legend, the reader is referred to the Web version of this article.)

diagram impossible as the relative importance of both effects on the system stability is currently unknown. Therefore, the first examples that are discussed affect a limited amount of physical attributes and their effects on polymer formation rate and system susceptibility to instability can be clearly distinguished. When moving to subsequent examples, the treated synthesis conditions affect progressively more physical attributes and the effects on both polymer formation rate and system susceptibility to instability become more convoluted. However, the overarching concept remains valid - the higher the positive effect predicted effect on (both) polymer formation rate and system susceptibility to instability, the greater the probability to form morphological features.

3.1.1. Supported vs unsupported

Conventional, supported IP vs an unsupported configuration is a relatively simple starting point, where both cases are performed under identical conditions except for variations of monomer concentrations. As a quantitative proxy to the polymer formation rate, the initial amine flux (Eq. (1)) is calculated using the reported values of monomer concentrations varied during IP and compared for experiments split into two cases – supported and unsupported. In these calculations, the diffusion coefficient for MPD in hexane, D_0, was estimated by multiplying its value in decane, as reported by Nowbahar et al. [70], with the viscosity ratio between hexane and decane. The partitioning coefficient, K, was taken from Behera et al. [32]. Details can be found in SI.

As shown in Fig. 8, the initial amine flux data are placed in the phase diagram, sorted into two columns, with the points calculated for the supported IP placed on the right, corresponding with the hypothesized increased susceptibility to instability (see sections 2.2.1, 2.2.2, the support acts as a 'disturbance'). Next to each point is an SEM image taken from the relevant paper. Finally, the data points are categorized by marker color/shape as introduced earlier in the phase diagram (Fig. 4), corresponding with the morphology seen in the SEM image. It is noted that all cases considered consist of MPD and TMC as monomers, in water and hexane, respectively, with the exception of the point shown for the

highest initial amine flux in the supported case, which was prepared using Isopar E (Fig. 8).

As may clearly be seen, presenting the data in this fashion lends strong support to the suggested framework: moving up along the y-axis, in the direction of increased formation rate, the system transitions from smooth to crumpled morphology. Furthermore, under conditions corresponding with similar formation rates, moving to the right on the x-axis from the unsupported to the supported system, the morphology also transitions from smooth to crumpled. The comparison of unsupported vs supported systems provides a strong support to the notion that the support impacts IP via the inherent heterogeneity it imparts to the system. The transitions between a smooth, crumpled and multi-layered morphology occur at higher values of initial amine flux for the unsupported system, which was defined as being inherently more stable than the supported system. This trend is schematically represented on the phase diagram by two arrows, each showing the transition for one of the systems. It is noted that Isopar E has a higher viscosity and higher interfacial tension with water compared to hexane, leading to lower partitioning and diffusion of MPD. Both would lead to a less pronounced morphology compared to what is expected if hexane would have been used. Consequently, the more crumpled (multi-layered) morphology seen here is an outcome of the increased monomer concentration and not the solvent change.

Previous conclusions appear to be also valid when comparing supported systems with varying pore sizes and pore densities (Fig. 9). The supports compared here are: an inorganic Al_2O_3 support with pore size of 2000 nm [56], a polycarbonate track-etched support with pore size of 50 nm [85], sacrificial nanostrand layer with pore size of 2 nm [22] and typical supports fabricated via phase inversion, with pore sizes varying between 2 and 100 nm [30,52,65]. The pore densities of phase inversion supports were estimated to be $> 10^9$ cm^2, based on pore sizes of 5–30 nm and surface porosities of 0.5–5% [53,82,87,99–101].

Positioning of the supports along the x-axis once again follows the logic of the phase diagram, with the notion that the porous morphology
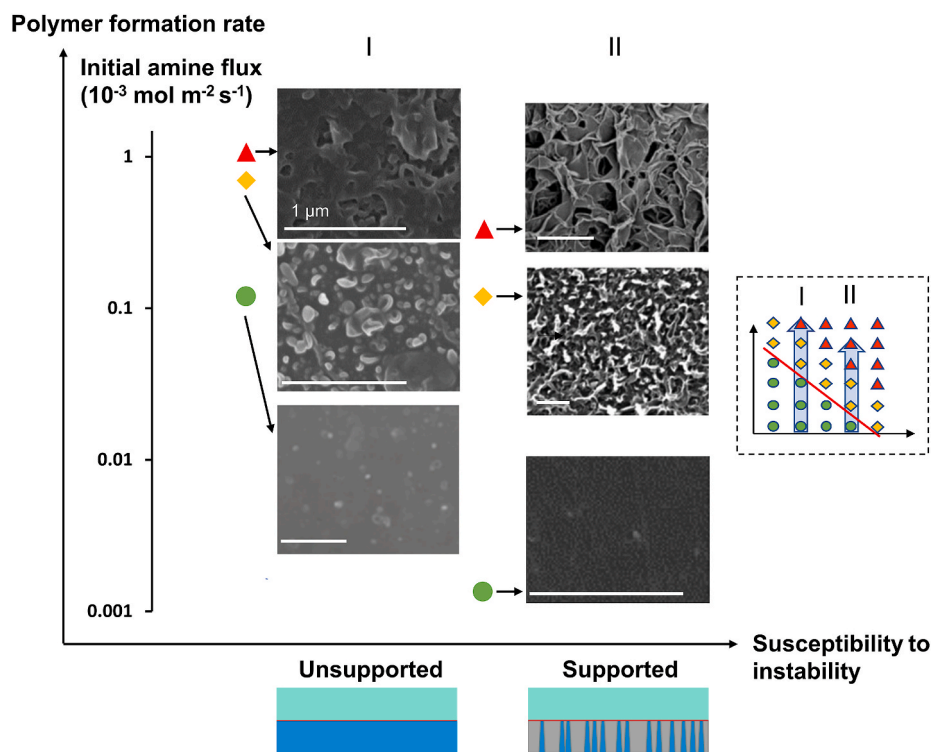

Fig. 8. Comparison of supported vs unsupported PA films prepared at increasing initial amine flux. The location of the symbols (triangle, diamond, and circle) is in accordance with the calculated initial amine flux. Inset: representation of evolution of morphology of both systems on the phase diagram as introduced by the framework in this paper. SEM images are taken from: (I) Jiang et al. [9] and (II) Ma et al. [30], Hermans et al. [52], Xu et al. [65]. Scale bar is 1 μm.
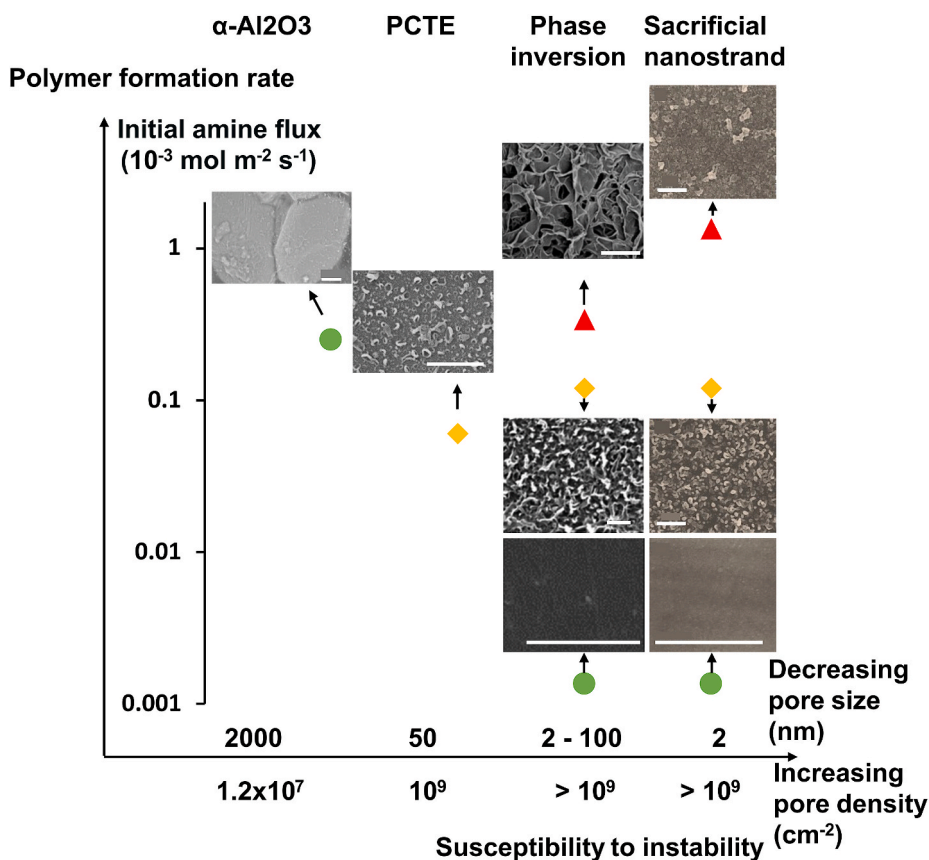
Fig. 9. Comparison of PA films, formed on different supports with increasing initial amine flux. Dataset consists of: an inorganic Al_2O_3 support with pore size 2000 μm [56], polycarbonate track-etched support with pore size of 50 nm [85], sacrificial nanostrand layer with pore size of 2 nm [22] and phase inversion supports with pore sizes between 2 and 100 nm [30,52,65]. Scale bar is 1 μm.

of the support serves as a 'wavelength' of the disturbance made to the initial state of the system. Here, it is hypothesized that small-scale heterogeneity (smaller pore size and/or higher pore density) makes the system more prone to become crumpled, manifested in a high-frequency disturbance (short wavelength cfr. section 2.2.2). As a result, at a similar initial amine flux, the PA layer becomes progressively rougher with decreasing pore size and increasing pore density (corresponding to moving from left to right in Fig. 9), being progressively less stable systems. The PCTE supports are characterized by a relatively low porosity, too low to produce a fully formed PA film [85]. The resulting film is rough but spatially heterogeneous, clearly indicating hotspots of reaction near pore sites [85]. The inorganic support contains micrometer-sized pores which makes the system locally similar to unsupported conditions, explaining the smooth morphology of the PA film. Both the sacrificial nanostrand layer and the phase inversion supports are characterized by small pores and higher porosity, and both systems result in similar film morphologies. It should be noted that, here, wetting is not accounted for (which could affect MPD supply due to different interactions with the support material) and neither is the thickness of the supports (thicker supports increase the sustainment of the reaction) since these data are lacking in the original references. Other differences in synthesis protocols between the selected membranes consist of different types of post-heat treatment (which is expected to alter performance rather than morphology) and different reaction times ranging from 60 to 120 s (which are the conventional reaction times and are considered to not significantly impact the morphology) and 10 min for the sacrificial nanostrand case with the lowest initial amine flux (which shows that these extremely low concentrations would need even longer reaction times to possibly become unstable) (Table S2).

3.1.2. Coating technique

Next, comparison of the effects of coating techniques on membrane morphology is highlighted. Coating techniques refer to different methods used to apply and contact the aqueous and organic phase in order to execute IP. Three main effects on system stability are identified. (I) Differences in the total amount of reactive monomers that are contacted (e.g. aqueous and organic phase are supplied as layers of several hundreds of micrometers [59] or nanometers, as bulk solutions [60] or as fine droplets [62]) which impact the sustainment of the reaction (Fig. 5). (II) The distance between the reaction interface and the underlying support on one hand and the atmosphere on the other hand (e. g. when fine droplets or thin liquid layers are used versus bulk solution and saturated supports). The former determines the initial susceptibility to instability of the system (Fig. 5, section 3.1.1). The latter might enhance overall heat dissipation and increase the overall system stability if, for example, fine droplets are used. (III) The monomer concentrations used, affecting the polymer formation rate (Fig. 5). It was found that the larger the distance between the IP reaction interface and the underlaying support, the lower the susceptibility to instability. The smaller the total amount of monomers supplied, the lower the sustainment of the reaction. Both are equivalent to smoother PA films. Again, for a single coating technique, lower initial amine fluxes resulted in formation of smoother films. The conclusions align with the framework proposed in this work. The extensive analysis of this example is included in the SI since details of the supports (porosity, pore density, wetting, thickness etc.) are unknown that might complicate a more accurate and rigorous comparison.

3.2. Simultaneous enhancement of both polymer formation rate and susceptibility to instability
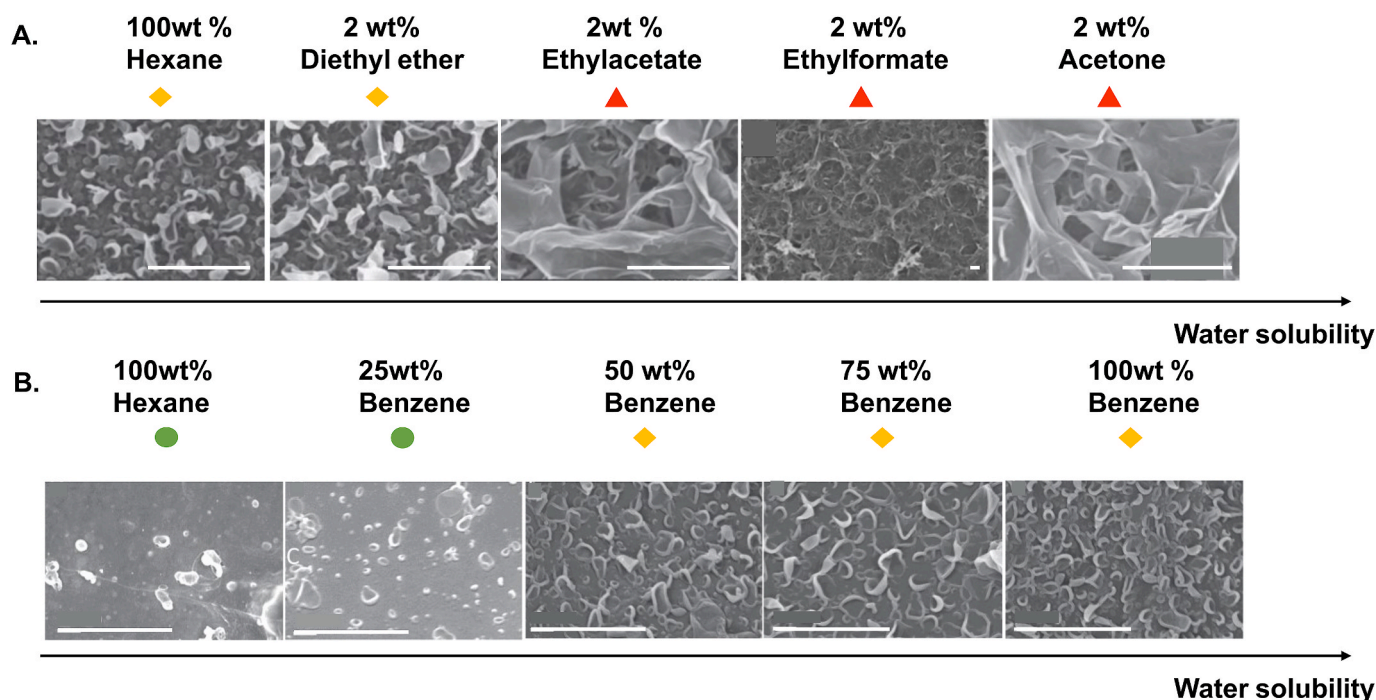
3.2.1. Co-solvents

The conventional water-hexane system is characterized by a large immiscibility gap over the entire composition range [102]; therefore, the IP reaction zone is very narrow [95]. Addition of co-solvents with higher water solubility compared to hexane will presumably increase its thickness [103] as the interfacial tension between the resulting aqueous and organic phase decreases, and the MPD diffusion rate into the reaction zone and equilibrium MPD partitioning increase [50,104]. The increase in MPD concentration in the reaction zone enhances the polymer formation rate (Eq. (1)), while the reduced interfacial tension increases the system susceptibility to instability (Figs. 5 and 6). The increase in both categories would result in a (qualitatively) diagonal line on the phase diagram (Fig. 4). However, the slope cannot be quantified at this point, since their relative importance is unknown. Still, as the co-solvent of interest enhances miscibility between aqueous and non-aqueous phase, both phenomena are positively influenced and thus a more pronounced film morphology is expected, up to the emergence of a multilayered structure.

Fig. 10A shows the resultant film morphology upon addition of different co-solvents at equal weight percentage (the molar concentrations range between 2.3 and 2.8 mM) to the hexane phase [105,106]. Closely examining the data, it is apparent that the co-solvents used differ in their water solubility (Table S4). As seen in Fig. 10A, the top-layer morphologies are very different, despite the identical monomer concentrations used. When moving from left to right, corresponding with increasing co-solvent water solubility, the morphology becomes more pronounced. Addition of diethyl ether, with the lowest water solubility, results in a crumpled film with larger ridges, whereas acetone, with the highest water solubility, results in a multilayered film. The same co-solvents as in Fig. 10A were tested separately at increased concentrations in hexane. It is clearly seen that the morphology becomes more pronounced as the co-solvent concentration increases, increasing the water solubility of the organic phase (Fig. S5 (a),(b),(c),(d)).

Similarly, when the benzene fraction is progressively increased in the organic phase (benzene is > 100x more water soluble than hexane, see Table S4), the film morphology changes from smooth (0–25 wt% benzene) to crumpled (~50–100 wt% benzene) (Fig. 10B) [104]. Curiously, the morphology does not become multilayered, as is seen in Fig. 10A, and this may be attributed to several reasons. First, in this example, the PA layer was prepared on top of a hydrogel support, which is expected to reduce the intensity of the IP reaction by facilitating slower, more homogeneous interfacial mass transfer, compared with a conventional support. Hence, the system's susceptibility to instability is lower than for phase inversion polymeric supports (data in Fig. 10A). Secondly, the polymer formation rate is lower (owing to reduced aqueous MPD diffusion), which also increases system stability. Finally, we note that the miscibility of benzene with water is lower compared to the co-solvents used in the data shown in Fig. 10A.

Besides changing the miscibility of the aqueous and organic phases, addition of co-solvents alters the boiling point of the organic phase, changing the system's susceptibility to instability via bubble formation. Recently, Peng et al. [86] stated that the reduction in boiling point upon addition of a co-solvent could result in interfacial vaporization, which then generates the enhanced roughness associated with co-solvent addition. The series shown in Fig. 10A, however, does not directly support this statement as the boiling point of diethyl ether (Table S4) is the lowest within this series but requires the highest concentration to form a multilayered film morphology (Fig. S5) [105]. Additionally, ethyl acetate is characterized by the highest boiling point (Table S4) but induces a multilayered morphology when added as 2 wt%. All co-solvents within this series, however, do show a lower boiling point than pristine hexane except for ethyl acetate (Table S4). Therefore, based on the presented dataset, reduction of boiling point cannot be the sole determinant for enhancing top-layer morphology for these co-solvent cases. Indeed, also addition of benzene to the organic phase induces a transition from smooth to crumpled morphology (Fig. 10B) despite its higher boiling point, compared with that of hexane (Table S4).

In conclusion, (co-)solvents clearly affect multiple physical attributes of the IP system and increase both initial amine flux and system

Fig. 10. The effect of co-solvent addition on the resultant film morphology. (A.) Addition of 2 wt% of various co-solvents, with varying water solubility, to the organic phase. Membranes are prepared via dip-coating on a phase inversion support. (B.) Addition of different concentrations of benzene to the organic phase. Membranes are prepared via dip-coating on an agarose hydrogel support [104–106]. Scale bar is 1 μm.

susceptibility to instability. Consequently, lumping them into a single category (co-solvents) can create an incoherent comparison in terms of the resultant effect on film properties. In order to understand the effect of singular physical attribute on IP and film morphology systematic experimental design should be performed.

3.2.2. Surfactants

Another class of additives reported in the literature, are surfactants, which may be added to IP to decrease the interfacial tension between the aqueous and organic phases [107]. Reduced interfacial tension increases the system susceptibility to instability as it makes the interface easier to deform. It is also speculated that it may facilitate initial partitioning of MPD into the organic phase, thus enhancing the polymer formation rate (Figs. 5 and 7). According to the suggested framework, increasing either or both of these two categories (formation rate and susceptibility) is expected to lead to a more crumpled morphology. The data shown in Fig. 11 are in agreement with the framework as the morphology of the formed PA film shifts with increasing SDS concentration, from smooth (for SFIP [58]) or from crumpled (for PE supported [67]) to multilayered.

3.2.3. Initial pH

As introduced in section 2.2.2 (Table S1), pH affects the fraction of unprotonated MPD (i.e. the most reactive form of MPD towards TMC) in the aqueous phase. By reducing the initial pH to values near or below the first acidity constant ($pKa_1 = 4.88$) of MPD, significantly less unprotonated MPD is present (Table S1). Therefore, the *actual* initial amine flux will be lower. Recalling the results shown in Fig. 8, a less pronounced morphology is expected if the initial pH of the aqueous solution is decreased. A lower initial pH also decreases the initial equilibrium solubility of CO_2 in the aqueous phase [109], therefore reducing the potential of the system for degassing upon initiation of the reaction (initial susceptibility to instability) thus leading to less formation of prominent morphological features. This is not to be confused by the dynamic effect of pH reduction during IP that facilitates CO_2 degassing and thus formation of morphological features (dynamic susceptibility to instability). On the other hand, a pH higher than the third acidity constant of CO_2

($pKa_3 = 10.3$), increases the initial equilibrium solubility of CO_2. However, less degassing is expected since the carbonate ion is the dominant species and uptake of protons does not directly lead to degassing [109]. The series of SEM images of membranes prepared with decreasing initial pH (Fig. 12) and, therefore, decreasing initial amine flux, show a changing top-layer morphology from a ridge and valley type, over nodules and leaves to solely nodular. No significant change in top-layer morphology is seen for pH values equal to or higher than 6, corresponding to an unprotonated fraction of MPD of at least 90% (Table S1). Once the pH is reduced to 5, a significant reduction in morphological features is seen, as only 57% of the bulk MPD concentration is in its unprotonated form. Apart from the explanation introduced by Peng et al. [109], based on degassing of CO_2, the results also correlate with the initial amine flux. Therefore, both the polymer formation rate and system susceptibility to instability are considered to be determining factors in the resultant morphology.

Finally, the dual effect of $NaHCO_3$ attributed to both buffering and degassing is discussed in the SI.

4. Conclusions

The present work outlines a unifying, physics-based framework for the synthesis-morphology relationship of polyamide TFC membranes. Within this framework, IP is considered as a system that may remain stable or become unstable during the course of the reaction. It is hypothesized that a stable system results in a smooth PA film, whereas an unstable system results in the formation of morphological features, such as crumpled or multilayered PA films. The system's stability is dictated by the synthesis conditions chosen for IP. Within the proposed framework, synthesis conditions are translated to their physical attributes relevant to IP, and ultimately expressed by two generalized system properties: 'polymer formation rate' and 'susceptibility to instability'. These two properties together dictate the stability of the system, linked to the resultant film morphology via a phase diagram, thereby connecting synthesis conditions to film morphology. The transition from a stable to unstable state (i.e. from smooth to crumpled/multilayered film) is governed by several destabilizing phenomena at the interface, driven
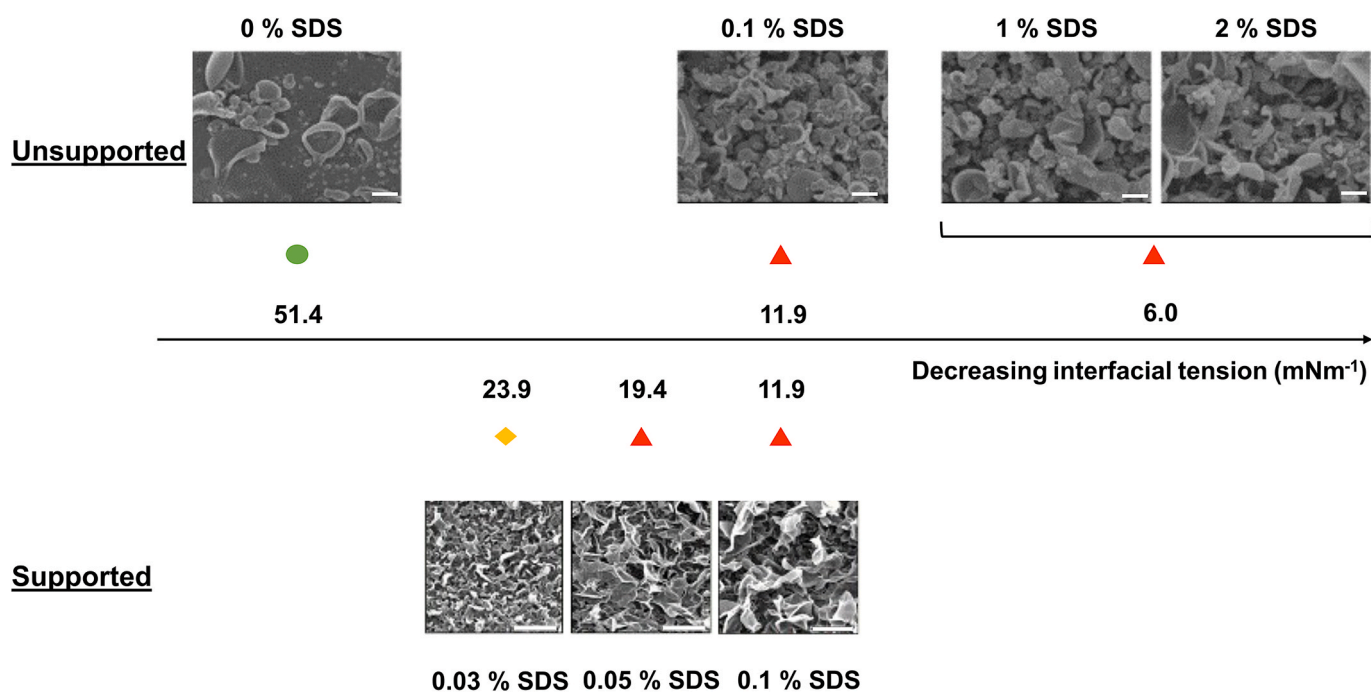

Fig. 11. The effect of SDS addition to the aqueous phase (plotted as reduced interfacial tension on the x-axis) on the resultant film morphology for both supported [67] and unsupported [58] membranes. Interfacial tension values are values between water and hexane upon addition of sodium dodecyl sulfonate (SDS), taken from Liang et al. [108]. Scale bar is 1 μm.
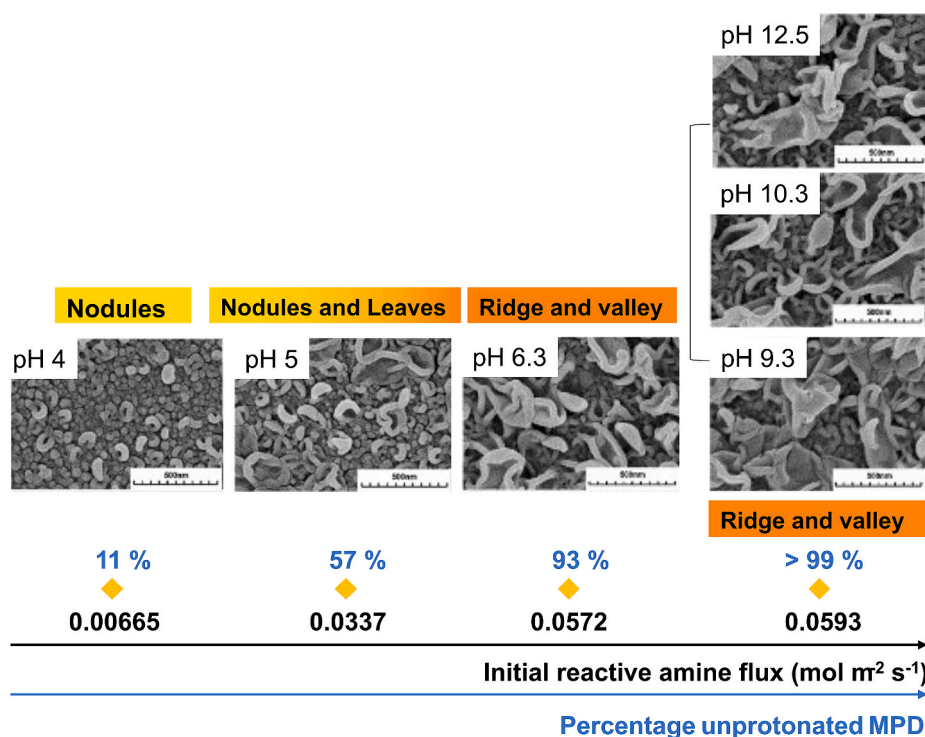
Fig. 12. Comparison of PA films prepared at different initial aqueous pH values and thus changing initial amine flux. Data from Peng et al. [109]. Scale bar is 500 nm.

by key characteristics of the reaction, namely: heat release, acid release, fast reaction kinetics and spatially heterogeneous polymer growth.

Our hypothesis, and the proposed framework, were tested using literature data. It was clearly shown that stable systems (lower 'polymer formation rate' and/or 'susceptibility to instability') exhibited smoother morphologies, whereas for unstable systems (higher 'polymer formation rate' and/or 'susceptibility to instability') the resultant film morphology was crumpled/multilayered. Future extensions of this work will require refined experimental design to focus on changing specific physical attributes of the IP reaction and study their effect on the system stability by the resultant film morphology. These concepts can also be extended to other types of IP involving different chemistries, e.g. epoxide-based. More detailed morphological characterization (of void size, surface area, interconnectivity) by techniques other than SEM, such as electron tomography, could help improve our understanding of the link between synthesis and morphology and ultimately performance. Furthermore, developing theoretical, model-based quantification of IP will provide insight into the stability threshold and its sensitivity to various physical attributes of IP. A rigorous understanding of the synthesis-morphology relationship will provide us with better tools for designing improved, tailor-made membranes.

CRediT authorship contribution statement

Ines Nulens: Conceptualization, Methodology, Data curation, Writing – original draft, Writing – review & editing, Visualization, Project administration. **Adi Ben Zvi:** Conceptualization, Methodology, Data curation, Writing – original draft, Writing – review & editing, Visualization, Project administration. **Ivo F.J. Vankelecom:** Supervision, Funding acquisition, Writing – review & editing. **Guy Z. Ramon:** Conceptualization, Methodology, Supervision, Funding acquisition, Writing – review & editing.

Declaration of competing interest

The authors declare that they have no known competing financial interests or personal relationships that could have appeared to influence the work reported in this paper.

Acknowledgements

References

[1] M. Elimelech, W.A. Phillip, The future of seawater desalination: energy, technology, and the environment, Science 333 (2011) 712–717, https://doi.org/10.1126/science.1200488.

[2] M. Elimelech, The global challenge for adequate and safe water, J. Water Supply Res. Technol. - Aqua 55 (2006) 3–10, https://doi.org/10.2166/aqua.2005.064.

[3] N. Hanasaki, S. Fujimori, T. Yamamoto, S. Yoshikawa, Y. Masaki, Y. Hijioka, M. Kainuma, Y. Kanamori, T. Masui, K. Takahashi, S. Kanae, A global water scarcity assessment under Shared Socio-economic Pathways - Part 2: water availability and scarcity, Hydrol. Earth Syst. Sci. 17 (2013) 2393–2413, https://doi.org/10.5194/hess-17-2393-2013.

[4] M.A. Shannon, P.W. Bohn, M. Elimelech, J.G. Georgiadis, B.J. Marĩas, A. M. Mayes, Science and technology for water purification in the coming decades, Nature 452 (2008) 301–310, https://doi.org/10.1038/nature06599.

[5] V.G. Gude, Desalination and water reuse to address global water scarcity, Rev. Environ. Sci. Biotechnol. 16 (2017) 591–609, https://doi.org/10.1007/s11157-017-9449-7.

[6] P.J.J. Alvarez, C.K. Chan, M. Elimelech, N.J. Halas, D. Villagrán, Emerging opportunities for nanotechnology to enhance water security, Nat. Nanotechnol. 13 (2018), https://doi.org/10.1038/s41565-018-0203-2.

[7] G.M. Geise, H.S. Lee, D.J. Miller, B.D. Freeman, J.E. Mcgrath, D.R. Paul, Water purification by membranes: the role of polymer science, J. Polym. Sci., Part B: Polym. Phys. 48 (2010) 1685–1718.

[8] W.D. Mulhearn, V.P. Oleshko, C.M. Stafford, Thickness-dependent permeance of molecular layer-by-layer polyamide membranes, J. Membr. Sci. 618 (2021), 118637, https://doi.org/10.1016/j.memsci.2020.118637.

[9] Z. Jiang, S. Karan, A.G. Livingston, Water transport through ultrathin polyamide nanofilms used for reverse osmosis, Adv. Mater. 30 (2018) 1–7, https://doi.org/10.1002/adma.201705973.

[10] M. Busch, W.E. Mickols, Reducing energy consumption in seawater desalination, Desalination 165 (2004) 299–312, https://doi.org/10.1016/j.desal.2004.06.035.

[11] E.M. Vrijenhoek, S. Hong, M. Elimelech, Influence of membrane surface properties on initial rate of colloidal fouling of reverse osmosis and nanofiltration membranes, J. Membr. Sci. 188 (2001) 115–128, https://doi.org/ S0376-7388(01)00376-3.

[12] C.Y. Tang, Y.N. Kwon, J.O. Leckie, Effect of membrane chemistry and coating layer on physiochemical properties of thin film composite polyamide RO and NF membranes. II. Membrane physiochemical properties and their dependence on polyamide and coating layers, Desalination 242 (2009) 168–182, https://doi.org/ 10.1016/j.desal.2008.04.004.

[13] R. Verbeke, V. Gómez, I.F.J. Vankelecom, Chlorine-resistance of reverse osmosis (RO) polyamide membranes, Prog. Polym. Sci. 72 (2017) 1–15, https://doi.org/10.1016/j.progpolymsci.2017.05.003.

[14] J.R. Werber, C.O. Osuji, M. Elimelech, Materials for next-generation desalination and water purification membranes, Nat. Rev. Mater. 1 (2016), https://doi.org/10.1038/natrevmats.2016.18.

[15] H. Ozaki, H. Li, Rejection of organic compounds by ultra-low pressure reverse osmosis membrane, Water Res. 36 (2002) 123–130, https://doi.org/10.1016/S0043-1354(01)00197-X.

[16] Y. Miyashita, S.H. Park, H. Hyung, C.H. Huang, J.H. Kim, Removal of n-nitrosamines and their precursors by nanofiltration and reverse osmosis membranes, J. Environ. Eng. 135 (2008) 788–795, https://doi.org/10.1061/(asce)ee.1943-7870.0000043.

[17] J.R. Werber, A. Deshmukh, M. Elimelech, The critical need for increased selectivity, not increased water permeability, for desalination membranes, Environ. Sci. Technol. Lett. 3 (2016) 112–120, https://doi.org/10.1021/acs.estlett.6b00050.

[18] G.M. Geise, H.B. Park, A.C. Sagle, B.D. Freeman, J.E. McGrath, Water permeability and water/salt selectivity tradeoff in polymers for desalination, J. Membr. Sci. 369 (2011) 130–138, https://doi.org/10.1016/j.memsci.2010.11.054.

[19] Z. Ali, Y. Wang, W. Ogieglo, F. Pacheco, H. Vovusha, Y. Han, I. Pinnau, Gas separation and water desalination performance of defect-free interfacially polymerized para-linked polyamide thin-film composite membranes, J. Membr. Sci. 618 (2021) 118–572, https://doi.org/10.1016/j.memsci.2020.118572.

[20] S. Hermans, H. Mariën, C. Van Goethem, I.F. Vankelecom, Recent developments in thin film (nano)composite membranes for solvent resistant nanofiltration, Curr. Opin. Chem. Eng. 8 (2015) 45–54, https://doi.org/10.1016/j.coche.2015.01.009.

[21] P. Vandezande, L.E.M. Gevers, I.F.J. Vankelecom, Solvent resistant nanofiltration: separating on a molecular level, Chem. Soc. Rev. 37 (2008) 365–405, https://doi.org/10.1039/b610848m.

[22] S. Karan, Z. Jiang, A.G. Livingston, Sub–10 nm polyamide nanofilms with ultrafast solvent transport for molecular separation, Science 348 (2015) 1347–1351.

[23] J. Wu, Q. Dai, H. Zhang, X. Li, Recent development in composite membranes for flow batteries, ChemSusChem 13 (2020) 3805–3819, https://doi.org/10.1002/cssc.202000633.

[24] Q. Dai, Z. Liu, L. Huang, C. Wang, Y. Zhao, Q. Fu, A. Zheng, H. Zhang, X. Li, Thin- film composite membrane breaking the trade-off between conductivity and selectivity for a flow battery, Nat. Commun. 11 (2020) 1–9, https://doi.org/10.1038/s41467-019-13704-2.

[25] G.M. Geise, D.R. Paul, B.D. Freeman, Fundamental water and salt transport properties of polymeric materials, Prog. Polym. Sci. 39 (2014) 1–42, https://doi.org/10.1016/j.progpolymsci.2013.07.001.

[26] S.P. Nunes, P.Z. Culfaz-Emecen, G.Z. Ramon, T. Visser, G.H. Koops, W. Jin, M. Ulbricht, Thinking the future of membranes: perspectives for advanced and new membrane materials and manufacturing processes, J. Membr. Sci. 598 (2020), 117761, https://doi.org/10.1016/j.memsci.2019.117761.

[27] L. Lin, R. Lopez, G.Z. Ramon, O. Coronell, Investigating the void structure of the polyamide active layers of thin-film composite membranes, J. Membr. Sci. 497 (2016) 365–376, https://doi.org/10.1016/j.memsci.2015.09.020.

[28] S. Mondal, I.M. Griffiths, G.Z. Ramon, Forefronts in structure-performance models of separation membranes, J. Membr. Sci. 588 (2019), 117166, https://doi.org/10.1016/j.memsci.2019.06.006.

[29] B. Ukrainsky, G.Z. Ramon, Temperature measurement of the reaction zone during polyamide film formation by interfacial polymerization, J. Membr. Sci. 566 (2018) 329–335, https://doi.org/10.1016/j.memsci.2018.09.011.

[30] X.H. Ma, Z.K. Yao, Z. Yang, H. Guo, Z.L. Xu, C.Y. Tang, M. Elimelech, Nanofoaming of polyamide desalination membranes to tune permeability and selectivity, Environ. Sci. Technol. Lett. 5 (2018) 123–130, https://doi.org/10.1021/acs.estlett.8b00016.

[31] Z. Tan, S. Chen, X. Peng, L. Zhang, C. Gao, Polyamide membranes with nanoscale turing structures for water purification, Science 360 (2018) 518–521, https://doi.org/10.1126/science.aar6308Turing.

[32] S. Behera, A.K. Suresh, Kinetics of interfacial polycondensation reactions – development of a new method and its validation, Polymer 127 (2017) 28–44, https://doi.org/10.1016/j.polymer.2017.08.026.

[33] M. Wang, C.M. Stafford, L.M. Cox, A.K. Blevins, M. Aghajani, J.P. Killgore, Y. Ding, Controlled growth of polyamide films atop homogenous and heterogeneous hydrogels using gel–liquid interfacial polymerization, Macromol. Chem. Phys. 220 (2019) 1–11, https://doi.org/10.1002/macp.201900100.

[34] I.J. Roh, Influence of rupture strength of interfacially polymerized thin-film structure on the performance of polyamide composite membranes, J. Membr. Sci. 198 (2002) 63–74, https://doi.org/10.1016/S0376-7388(01)00630-5.

[35] H. Mariën, I.F.J. Vankelecom, Optimization of the ionic liquid-based interfacial polymerization system for the preparation of high-performance, low-fouling RO membranes, J. Membr. Sci. 556 (2018) 342–351, https://doi.org/10.1016/j.memsci.2018.03.071.

[36] M.J.T. Raaijmakers, N.E. Benes, Current trends in interfacial polymerization chemistry, Prog. Polym. Sci. 63 (2016) 86–142, https://doi.org/10.1016/j.progpolymsci.2016.06.004.

[37] Y. Yao, P. Zhang, C. Jiang, R.M. DuChanois, X. Zhang, M. Elimelech, High performance polyester reverse osmosis desalination membrane with chlorine resistance, Nat. Sustain. 4 (2021) 138–146, https://doi.org/10.1038/s41893-020-00619-w.

[38] R. Zhang, S. Yu, W. Shi, W. Wang, X. Wang, Z. Zhang, L. Li, B. Zhang, X. Bao, A novel polyesteramide thin film composite nanofiltration membrane prepared by interfacial polymerization of serinol and trimesoyl chloride (TMC) catalyzed by 4-dimethylaminopyridine (DMAP), J. Membr. Sci. 542 (2017) 68–80, https://doi.org/10.1016/j.memsci.2017.07.054.

[39] M. Liu, Y. Zheng, S. Shuai, Q. Zhou, S. Yu, C. Gao, Thin-film composite membrane formed by interfacial polymerization of polyvinylamine (PVAm) and trimesoyl chloride (TMC) for nanofiltration, Desalination 288 (2012) 98–107, https://doi.org/10.1016/j.desal.2011.12.018.

[40] S. Yu, M. Liu, X. Liu, C. Gao, Performance enhancement in interfacially synthesized thin-film composite polyamide-urethane reverse osmosis membrane for seawater desalination, J. Membr. Sci. 342 (2009) 313–320, https://doi.org/10.1016/j.memsci.2009.07.003.

[41] S.J. Park, W. Choi, S.E. Nam, S. Hong, J.S. Lee, J.H. Lee, Fabrication of polyamide thin film composite reverse osmosis membranes via support-free interfacial polymerization, J. Membr. Sci. 526 (2017) 52–59, https://doi.org/10.1016/j.memsci.2016.12.027.

[42] Y. Jin, Z. Su, Effects of polymerization conditions on hydrophilic groups in aromatic polyamide thin films, J. Membr. Sci. 330 (2009) 175–179, https://doi.org/10.1016/j.memsci.2008.12.055.

[43] G.E. Chen, Y.J. Liu, Z.L. Xu, Y.J. Tang, H.H. Huang, L. Sun, Fabrication and characterization of a novel nanofiltration membrane by the interfacial polymerization of 1,4-diaminocyclohexane (DCH) and trimesoyl chloride (TMC), RSC Adv. 5 (2015) 40742–40752, https://doi.org/10.1039/c5ra02560e.

[44] A.K. Ghosh, B.H. Jeong, X. Huang, E.M.V. Hoek, Impacts of reaction and curing conditions on polyamide composite reverse osmosis membrane properties, J. Membr. Sci. 311 (2008) 34–45, https://doi.org/10.1016/j.memsci.2007.11.038.

[45] Y. Mansourpanah, S.S. Madaeni, A. Rahimpour, H.S. Afarani, Using different surfactants for changing the properties of poly(piperazineamide) TFC nanofiltration membranes, Desalination 271 (2011) 169–177, https://doi.org/10.1016/j.desal.2010.12.026.

[46] Y. Mansourpanah, S.S. Madaeni, A. Rahimpour, Fabrication and development of interfacial polymerized thin-film composite nanofiltration membrane using different surfactants in organic phase; study of morphology and performance, J. Membr. Sci. 343 (2009) 219–228, https://doi.org/10.1016/j.memsci.2009.07.033.

[47] B. Khorshidi, T. Thundat, D. Pernitsky, M. Sadrzadeh, A parametric study on the synergistic impacts of chemical additives on permeation properties of thin film composite polyamide membrane, J. Membr. Sci. 535 (2017) 248–257, https://doi.org/10.1016/j.memsci.2017.04.052.

[48] W. Fang, L. Shi, R. Wang, Interfacially polymerized composite nanofiltration hollow fiber membranes for low-pressure water softening, J. Membr. Sci. 430 (2013) 129–139, https://doi.org/10.1016/j.memsci.2012.12.011.

[49] I.C. Kim, B.R. Jeong, S.J. Kim, K.H. Lee, Preparation of high flux thin film composite polyamide membrane: the effect of alkyl phosphate additives during interfacial polymerization, Desalination 308 (2013) 111–114, https://doi.org/10.1016/j.desal.2012.08.001.

[50] C. Kong, T. Shintani, T. Kamada, V. Freger, T. Tsuru, Co-solvent-mediated synthesis of thin polyamide membranes, J. Membr. Sci. 384 (2011) 10–16, https://doi.org/10.1016/j.memsci.2011.08.055.

[51] Z. Zhang, Y. Qin, G. Kang, H. Yu, Y. Jin, Y. Cao, Tailoring the internal void structure of polyamide films to achieve highly permeable reverse osmosis membranes for water desalination, J. Membr. Sci. 595 (2020) 117–518, https://doi.org/10.1016/j.memsci.2019.117518.

[52] S. Hermans, R. Bernstein, A. Volodin, I.F.J. Vankelecom, Study of synthesis parameters and active layer morphology of interfacially polymerized polyamide – polysulfone membranes, React. Funct. Polym. 86 (2015) 199–208, https://doi.org/10.1016/j.reactfunctpolym.2014.09.013.

[53] J.A.D. Sharabati, S. Guclu, S. Erkoc-Ilter, D.Y. Koseoglu-Imer, S. Unal, Y. Z. Menceloglu, I. Ozturk, I. Koyuncu, Interfacially polymerized thin-film composite membranes: impact of support layer pore size on active layer polymerization and seawater desalination performance, Separ. Purif. Technol. 212 (2019) 438–448, https://doi.org/10.1016/j.seppur.2018.11.047.

[54] M. Fathizadeh, A. Aroujalian, A. Raisi, Preparation and characterization of thin film composite reverses osmosis membranes with wet and dry support layer, Desalination Water Treat. 56 (2015) 2284–2295, https://doi.org/10.1080/19443994.2014.963159.

[55] Q. Zhang, Z. Zhang, L. Dai, H. Wang, S. Li, S. Zhang, Novel insights into the interplay between support and active layer in the thin film composite polyamide membranes, J. Membr. Sci. 537 (2017) 372–383, https://doi.org/10.1016/j.memsci.2017.05.033.

[56] Z. Zhou, D. Lu, X. Li, L.M. Rehman, A. Roy, Z. Lai, Fabrication of highly permeable polyamide membranes with large "leaf-like" surface nanostructures on inorganic supports for organic solvent nanofiltration, J. Membr. Sci. 601 (2020), https://doi.org/10.1016/j.memsci.2020.117932.

[57] Y. Li, E. Wong, A. Volodine, C. Van Haesendonck, K. Zhang, B. Van der Bruggen, Nanofibrous hydrogel composite membranes with ultrafast transport performance for molecular separation in organic solvents, J. Mater. Chem. (2019), https://doi.org/10.1039/C9TA06169J.

[58] Y. Cui, X.Y. Liu, T.S. Chung, Ultrathin polyamide membranes fabricated from free-standing interfacial polymerization: synthesis, modifications, and post-treatment, Ind. Eng. Chem. Res. 56 (2017) 513–523, https://doi.org/10.1021/acs.iecr.6b04283.

[59] S.J. Park, W.G. Ahn, W. Choi, S.H. Park, J.S. Lee, H.W. Jung, J.H. Lee, A facile and scalable fabrication method for thin film composite reverse osmosis membranes: dual-layer slot coating, J. Mater. Chem. A. 5 (2017) 6648–6655, https://doi.org/ 10.1039/c7ta00891k.

[60] X. Song, S. Qi, C.Y. Tang, C. Gao, Ultra-thin, multi-layered polyamide membranes: synthesis and characterization, J. Membr. Sci. 540 (2017) 10–18, https://doi.org/10.1016/j.memsci.2017.06.016.

[61] X. Wang, H. Ma, B. Chu, B.S. Hsiao, Thin-film nanofibrous composite reverse osmosis membranes for desalination, Desalination 420 (2017) 91–98, https://doi. org/10.1016/j.desal.2017.06.029.

[62] M.R. Chowdhury, J. Steffes, B.D. Huey, J.R. Mccutcheon, 3D printed polyamide membranes for desalination, Science 361 (2018) 682–686, https://doi.org/10.1126/science.aar2122.

[63] X.H. Ma, Z. Yang, Z.K. Yao, H. Guo, Z.L. Xu, C.Y. Tang, Interfacial polymerization with electrosprayed microdroplets: toward controllable and ultrathin polyamide membranes, Environ. Sci. Technol. Lett. 5 (2018) 117–122, https://doi.org/10.1021/acs.estlett.7b00566.

[64] B.S. Lalia, V. Kochkodan, R. Hashaikeh, N. Hilal, A review on membrane fabrication: structure, properties and performance relationship, Desalination 326 (2013) 77–95, https://doi.org/10.1016/j.desal.2013.06.016.

[65] J. Xu, H. Yan, Y. Zhang, G. Pan, Y. Liu, The morphology of fully-aromatic polyamide separation layer and its relationship with separation performance of TFC membranes, J. Membr. Sci. 541 (2017) 174–188, https://doi.org/10.1016/j.memsci.2017.06.057.

[66] I.J. Roh, A.R. Greenberg, V.P. Khare, Synthesis and characterization of interfacially polymerized polyamide thin films, Desalination 191 (2006) 279–290, https://doi.org/10.1016/j.desal.2006.03.004.

[67] S.H. Park, S.J. Kwon, M.G. Shin, M.S. Park, J.S. Lee, C.H. Park, H. Park, J.H. Lee, Polyethylene-supported high performance reverse osmosis membranes with enhanced mechanical and chemical durability, Desalination 436 (2018) 28–38, https://doi.org/10.1016/j.desal.2018.02.007.

[68] B. Khorshidi, T. Thundat, B.A. Fleck, M. Sadrzadeh, Thin film composite polyamide membranes: parametric study on the influence of synthesis conditions, RSC Adv. 5 (2015) 54985–54997, https://doi.org/10.1039/c5ra08317f.

[69] Z. Ali, Y. Al Sunbul, F. Pacheco, W. Ogieglo, Y. Wang, G. Genduso, I. Pinnau, Defect-free highly selective polyamide thin-film composite membranes for desalination and boron removal, J. Membr. Sci. 578 (2019) 85–94, https://doi.org/10.1016/j.memsci.2019.02.032.

[70] A. Nowbahar, V. Mansard, J.M. Mecca, M. Paul, T. Arrowood, T.M. Squires, Measuring interfacial polymerization kinetics using microfluidic interferometry, J. Am. Chem. Soc. 140 (2018) 3173–3176, https://doi.org/10.1021/jacs.7b12121.

[71] V. Freger, G.Z. Ramon, Polyamide desalination membranes: formation, structure, and properties, Prog. Polym. Sci. 122 (2021), 101451, https://doi.org/10.1016/j.progpolymsci.2021.101451.

[72] O. Coronell, B.J. Mariñas, D.G. Cahill, Depth heterogeneity of fully aromatic polyamide active layers in reverse osmosis and nanofiltration membranes, Environ. Sci. Technol. 45 (2011) 4513–4520, https://doi.org/10.1021/es200007h.

[73] V. Freger, Nanoscale heterogeneity of polyamide membranes formed by interfacial polymerization, Langmuir 19 (2003) 4791–4797, https://doi.org/10.1021/la020920q.

[74] V. Freger, S. Srebnik, Mathematical model of charge and density distributions in interfacial polymerization of thin films, J. Appl. Polym. Sci. 88 (2003) 1162–1169, https://doi.org/10.1002/app.11716.

[75] C.C. Wamser, M.I. Gilbert, Detection of surface functional group Asymmetry in interfacially-polymerized films by contact angle titrations, Langmuir (1992) 1608–1614.

[76] R.J. Petersen, Composite reverse osmosis and nanofiltration membranes, J. Membr. Sci. 83 (1993) 81–150, https://doi.org/10.1016/0376-7388(93)80014-O.

[77] M. Stolov, V. Freger, Membrane charge weakly affects ion transport in reverse osmosis, Environ. Sci. Technol. Lett. (2020), https://doi.org/10.1021/acs.estlett.0c00291.

[78] S.H. Kim, S.Y. Kwak, T. Suzuki, Positron annihilation spectroscopic evidence to demonstrate the flux-enhancement mechanism in morphology-controlled thin-film-composite (TFC) membrane, Environ. Sci. Technol. 39 (2005) 1764–1770, https://doi.org/10.1021/es049453k.

[79] V. Freger, Swelling and morphology of the skin layer of polyamide composite membranes : an atomic force microscopy study, Environ. Sci. Technol. 38 (2004) 3168–3175, https://doi.org/10.1021/es034815u.

[80] M. Stolov, V. Freger, Membrane charge weakly affects ion transport in reverse osmosis, Environ. Sci. Technol. Lett. 7 (2020) 440–445, https://doi.org/10.1021/acs.estlett.0c00291.

[81] D.L. Shaffer, K.E. Feldman, E.P. Chan, G.R. Stafford, C.M. Stafford, Characterizing salt permeability in polyamide desalination membranes using electrochemical impedance spectroscopy, J. Membr. Sci. 583 (2019) 248–257, https://doi.org/10.1016/j.memsci.2019.04.062.

[82] M.C.Y. Wong, L. Lin, O. Coronell, E.M.V. Hoek, G.Z. Ramon, Impact of liquid-filled voids within the active layer on transport through thin-film composite membranes, J. Membr. Sci. 500 (2016) 124–135, https://doi.org/10.1016/j.memsci.2015.11.033.

[83] X. Ma, Z. Yang, Z. Yao, H. Guo, Z. Xu, C.Y. Tang, Tuning roughness features of thin film composite polyamide membranes for simultaneously enhanced permeability, selectivity and anti-fouling performance, J. Colloid Interface Sci. 540 (2019) 382–388, https://doi.org/10.1016/j.jcis.2019.01.033.

[84] X. Song, B. Gan, S. Qi, H. Guo, C.Y. Tang, Y. Zhou, C. Gao, Intrinsic nanoscale structure of thin film composite polyamide membranes: connectivity, defects, and structure-property correlation, Environ. Sci. Technol. 54 (2020) 3559–3569, https://doi.org/10.1021/acs.est.9b05892.

[85] L.E. Peng, Z. Yao, Z. Yang, H. Guo, C.Y. Tang, Dissecting the role of substrate on the morphology and separation properties of thin film composite polyamide membranes: seeing is believing, Environ. Sci. Technol. 54 (2020) 6978–6986, https://doi.org/10.1021/acs.est.0c01427.

[86] L.E. Peng, Y. Jiang, L. Wen, H. Guo, Z. Yang, C.Y. Tang, Does interfacial vaporization of organic solvent affect the structure and separation properties of polyamide RO membranes, J. Membr. Sci. 625 (2021), 119173, https://doi.org/10.1016/j.memsci.2021.119173.

[87] X. Song, B. Gan, Z. Yang, C.Y. Tang, C. Gao, Confined nanobubbles shape the surface roughness structures of thin film composite polyamide desalination membranes, J. Membr. Sci. 582 (2019) 342–349, https://doi.org/10.1016/j.memsci.2019.04.027.

[88] P. Drazin, Computational Aerodynamics and Fluid Dynamics: an Introduction, 2002, https://doi.org/10.1017/CBO9780511809064.

[89] R. Patne, G.Z. Ramon, Stability of fluid flows coupled by a deformable solid layer, J. Fluid Mech. (2020), https://doi.org/10.1017/jfm.2020.774.

[90] F. Esfandian, M. Peyravi, A.A. Ghoreyshi, M. Jahanshahi, A.S. Rad, Fabrication of TFC nanofiltration membranes via co-solvent assisted interfacial polymerization for lactose recovery, Arab. J. Chem. 12 (2019) 5325–5338, https://doi.org/10.1016/j.arabjc.2017.01.004.

[91] L. Leal, Hydrodynamic Stability, Cambridge University Press, Cambridge, 2007, https://doi.org/10.1017/CBO9780511800245.013.

[92] J. Lee, A. Hill, S. Kentish, Formation of a thick aromatic polyamide membrane by interfacial polymerisation, Separ. Purif. Technol. 104 (2013) 276–283, https://doi.org/10.1016/j.seppur.2012.11.015.

[93] H.V. Moradi, J.M. Floryan, New instability mode in a grooved channel, J. Fluid Mech. 778 (2015) 691–720, https://doi.org/10.1017/jfm.2015.399.

[94] K. Grzebyk, M.D. Armstrong, O. Coronell, Accessing greater thickness and new morphology features in polyamide active layers of thin-film composite membranes by reducing restrictions in amine monomer supply, J. Membr. Sci. 644 (2022), 120112, https://doi.org/10.1016/j.memsci.2021.120112.

[95] V. Freger, Kinetics of film formation by interfacial polycondensation, Langmuir 21 (2005) 1884–1894, https://doi.org/10.1021/la048085v.

[96] M.L.V. Ramires, C.A. Nieto Castro, Y. Nagasaka, A. Nagashima, M.J. Assael, W. A. Wakeham, Standard reference data for the thermal conductivity of water, J. Phys. Chem. Ref. Data 24 (1995) 1377–1381, https://doi.org/10.1063/1.555963.

[97] Solvay Specialty Polymers, Udel® Polysulfone Design Guide, 2015, pp. 1–84.

[98] M.J. Assael, E. Charitidou, C.A.N. de Castro, W.A. Wakeham, The thermal conductivity of n-hexane, n-heptane, and n-decane by the transient hot-wire method, Int. J. Thermophys. 8 (1987) 663–670, https://doi.org/10.1007/BF00500786.

[99] G.Z. Ramon, M.C.Y. Wong, E.M.V. Hoek, Transport through composite membrane , part 1 : is there an optimal support membrane, J. Membr. Sci. 415–416 (2012) 298–305, https://doi.org/10.1016/j.memsci.2012.05.013.

[100] G.R. Guillen, T.P. Farrell, R.B. Kaner, E.M.V. Hoek, Pore-structure, hydrophilicity, and particle filtration characteristics of polyaniline-polysulfone ultrafiltration membranes, J. Mater. Chem. 20 (2010) 4621–4628, https://doi.org/10.1039/b925269j.

[101] S.Y. Kwak, D. Woo Ihm, Use of atomic force microscopy and solid-state NMR spectroscopy to characterize structure-property-performance correlation in high-flux reverse osmosis (RO) membranes, J. Membr. Sci. 158 (1999) 143–153, https://doi.org/10.1016/S0376-7388(99)00039-3.

[102] J. Acosta-Esquijarosa, I. Rodríguez-Donis, E. Pardillo-Fontdevila, Physical properties and their corresponding changes of mixing for the ternary mixture acetone + n-hexane + water at 298.15 K, Thermochim, Acta 443 (2006) 93–97, https://doi.org/10.1016/j.tca.2006.01.008.

[103] C. Kong, M. Kanezashi, T. Yamomoto, T. Shintani, T. Tsuru, Controlled synthesis of high performance polyamide membrane with thin dense layer for water desalination, J. Membr. Sci. 362 (2010) 76–80, https://doi.org/10.1016/j.memsci.2010.06.022.

[104] Z. Wang, S. Liang, Y. Jin, L. Zhao, L. Hu, Controlling structure and properties of polyamide nanofilms by varying amines diffusivity in organic phase, J. Membr. Sci. 574 (2019) 1–9, https://doi.org/10.1016/j.memsci.2018.12.036.

[105] T. Kamada, T. Ohara, T. Shintani, T. Tsuru, Optimizing the preparation of multi-layered polyamide membrane via the addition of a co-solvent, J. Membr. Sci. 453 (2014) 489–497, https://doi.org/10.1016/j.memsci.2013.11.028.

[106] Z. Liu, G. Zhu, Y. Wei, D. Zhang, L. Jiang, H. Wang, C. Gao, Enhanced flux performance of polyamide composite membranes prepared via interfacial polymerization assisted with ethyl formate, Water Sci. Technol. 76 (2017) 1884–1894, https://doi.org/10.2166/wst.2017.349.

[107] A.F. Belhaj, K.A. Elraies, M.S. Alnarabiji, J.A.B.M. Shuhli, S.M. Mahmood, L. W. Ern, Experimental investigation of surfactant partitioning in Pre-CMC and Post-CMC regimes for enhanced oil recovery application, Energies 12 (2019), https://doi.org/10.3390/en12122319.

[108] Y. Liang, Y. Zhu, C. Liu, K. Lee, W. Hung, Z. Wang, Y. Li, M. Elimelech, J. Jin, S. Lin, Polyamide nanofiltration membrane with highly uniform sub-nanometre pores for sub-1 Å precision separation, Nat. Commun. 11 (2020) 1–9, https://doi.org/10.1038/s41467-020-15771-2.

[109] L.E. Peng, Z. Yao, X. Liu, B. Deng, H. Guo, C.Y. Tang, Tailoring polyamide rejection layer with aqueous carbonate chemistry for enhanced membrane separation: mechanistic insights, chemistry-structure-property relationship, and environmental implications, Environ. Sci. Technol. 53 (2019) 9764–9770, https://doi.org/10.1021/acs.est.9b03210.